Pressure-Sensitive Paint Measurements and CFD Analysis of Vortex Flow in a Cyclone Separator

by
Nicola Lucarelli

Submitted in Partial Fulfillment of the Requirements
for the Degree of
Master of Science in Engineering
in the
Mechanical Engineering
Program

YOUNGSTOWN STATE UNIVERSITY
December, 2019

Pressure-Sensitive Paint Measurements and CFD
Analysis of Vortex Flow in a Cyclone Separator
Nicola Lucarelli

I hereby release this thesis to the public. I understand that this thesis will be made available from the OhioLINK ETD Center and the Maag Library Circulation Desk for public access. I also authorize the University or other individuals to make copies of this thesis as needed for scholarly research.

Signature:

Nicola Lucarelli, Student Date

Approvals:

Dr. Kevin Disotell, Thesis Advisor Date

Dr. Ștefan Moldovan, Committee Member Date

Dr. Kyosung Choo, Committee Member Date

Dr. Salvatore A. Sanders, Dean of Graduate Studies Date

Abstract

An analysis of the vortex flow in a particle filtration device, known as a cyclone separator, was performed via computational and experimental models. Optical measurements were taken using pressure-sensitive paint (PSP) to capture the pressure field along the cone of a cyclone separator. An in-situ calibration method was utilized to offset the error induced via viscous heating of the fluid. The pressure drop, captured with both physical wall pressure taps and through PSP measurements, was much lower than expected when compared to Shephard and Lapple pressure drop theory. Conversely, the pressure drop along the cone wall predicted in the closed configuration computational fluid dynamics (CFD) model agrees in magnitude with the experimental data, although a bulk shift in the pressure level is present.

Using a commercial computational fluid dynamics solver ANSYS Fluent, a Reynolds Stress Model was used to capture the anisotropic turbulence present in the cyclone separator. For computational analysis, two configurations were modeled. An open configuration, with a "once-through" vortex structure, was simulated and yielded drastically modified vortex flow characteristics compared to those from the literature. An additional closed configuration simulation was completed, which produced the typical reversed-flow vortex present in most cyclone separators. The results from the closed configuration model show good agreement with experimental and computational data from the literature.

The closed configuration model produced tangential velocities approximately two and a half times greater than the supplied inlet velocity with a corresponding velocity profile following the typical Rankine vortex expected in cyclone flow. Analysis of the form of the free-vortex flow shows the CFD results following an inverse-power law relation between tangential velocity and radial position within the ranges expected from the literature. Furthermore, inspection of the unsteadiness present in the flow shows peaks near the unsteady precessing vortex core (PVC). A helical structure is also present in the flow giving an indication of a periodic internal flow structure.

Acknowledgments

I would like to thank Dr. Disotell for his constant guidance and support through the thesis and research process. His instruction along with that from my committee members, Dr. Moldovan and Dr. Choo, has been instrumental in my understanding of the scientific investigative process. I am also grateful for the continuous input from the faculty and graduate students of the Mechanical, Industrial, and Manufacturing Engineering department.

I am incredibly grateful for my family, especially my parents, Franco and Joanne Lucarelli, who have given me constant support throughout my graduate career. The morals and work ethic which they have instilled in me have been instrumental in my development at Youngstown State University.

Finally, I would like to thank the Graduate School and Mechanical Engineering department for granting me a Graduate Assistantship for the duration of my studies, and giving me the opportunity to further my education while developing useful research skills.

Contents

List of Figures

List of Tables

Nomenclature

Variables

α	geometric parameter modeling flow contraction at the inlet
δ	Kronecker delta
ϵ	turbulent dissipation rate
$\frac{h}{R}$	relative wall roughness
Γ	angular momentum
γ	cone half angle
μ	dynamic viscosity
μ_t	turbulent viscosity
ν	kinematic viscosity
ω	angular velocity
ϕ_{ij}	pressure strain
ρ	fluid density
τ	luminescent lifetime
τ_w	shear stress at the wall
A	coefficient in Stern-Volmer relationship
a	inlet height
B	coefficient in Stern-Volmer relationship
b	inlet width
C	constant used in free-vortex formulation

c_o mass ratio solids loading factor

D cylinder diameter

D_d particle outlet diameter

D_x vortex finder diameter

$D_{L,ij}$ molecular diffusion

$D_{T,ij}$ turbulent diffusion

E time dependent illumination

E_x Euler number from the vortex finder

Eu Euler number across the entire system

Eu_{body} Euler number from the cyclone body

Eu_{in} Euler number from the cyclone inlet

f friction factor

f_θ body force in the azimuthal direction

f_r body force in the radial direction

f_z body force in the axial direction

f_{air} friction factor for "clean"

f_{cone} friction factor from cone

f_{dust} friction factor due to solids loading

F_{ij} system rotation

f_{lid} friction factor from cylinder lid

f_{PVC} frequency of precessing vortex core

H height of cyclone

h surface roughness

H_c height of cone section

H_v inlet velocity head

H_{cs}	height of Barth control surface
I	luminescent intensity
K	constant for use in Shepherd and Lapple pressure drop theory
k	turbulent kinetic energy
n	constant of free-vortex power law
p	static pressure
P_{ij}	stress production
Q	volumetric flow rate
R	cylinder radius
r	spatial coordinate in the radial direction
R_s	core radius in core pressure drop model
R_x	vortex finder radius
R_{cr}	critical radius in core pressure drop model
R_{in}	inlet centerline radius
Re	Reynolds number defined at cyclone inlet
Re_x	Reynolds number at vortex finder outlet
Re_{cyc}	cyclone Reynolds number
S	vortex finder length from the top of the cyclone
S_g	geometric swirl number
Sk	Stokes number
St	Strouhal number
t	time
u^*	friction velocity
v	fluid velocity
x_{50}	cut size relating to a 50% collection efficiency

y^+ nondimensional height normal to surface

Subscripts

θ indicates azimuthal direction

CS Indicates a quantity located at the control surface

i, j, k indicate orthogonal tensor directions

in indicates quantity at the cyclone inlet

ref indicates reference or wind-off condition

w indicates quantity located at the outer cyclone wall

z indicates axial direction

Superscripts

$'$ indicates fluctuating quantity

$*$ indicates "modified" quantity for use in Meissner and Löffler method

$\overline{\phi}$ an overbar indicates an averaged value for any quantity

Acronyms

CFD Computational Fluid Dynamics

DNS Direct Numerical Simulation

HEPA High Efficiency Particulate Air

LDA Laser Doppler Anemometry

LES Large Eddy Simulation

PM Particulate Matter

PSP Pressure Sensitive Paint

PtTFPP Pt(II) meso-tetrakis(pentafluorophenyl)porphine or platinum porphyrin

PVC Precessing Vortex Core

RANS Reynolds Averaged Navier-Stokes

RSM Reynolds Stress Model

SNR Signal-to-Noise Ratio

TLC Thin-layer Chromatography

Chapter 1. Introduction

1.1 Cyclone Separator

1.1.1 Centrifugal Separator Background

The cyclone separator is an incredibly robust device used primarily for filtration. With no moving parts, the design is simple yet effective in particulate separation. The separation of particles from the fluid they are embedded within can be done in many ways with inertial separation being one of the more popular ways. Inertial separators, in general, achieve filtration by changing the direction of the working fluid relative to the particles. In this way the particles pass over the fluid streamlines and are separated from the bulk flow. Cyclones are a subset of inertial separators that operate using vortex motion. Using centrifugal force as the separation mechanism, particles of higher density and sufficient diameter are separated from the fluid volume and expunged from the system. The processed fluid then exits the system where, depending on the particular application, it goes through a series of fabric (HEPA) filters to separate the remaining fine particulate.

The simple design of the cyclone separator allows for wide range of operating conditions and dimensions to fit the specific application at hand. For industrial applications such as sawmills and oil refineries, the cyclone separator can be quite large. Dependent on the operating conditions, cyclones can be tuned to filter a large range of particle diameters. In a sawmill, for example, the targeted particulate has a larger diameter, so high velocities are not critical. However, in oil refineries and industrial kitchens, the oil particulate trapped in the airflow can be small, which requires higher tangential velocities for separation. By adjusting the cyclone geometry and inlet conditions, the cyclone separator can act as an efficient filtration device in both of these scenarios. Cyclones are often rated for a given cut size which defines the particle diameter that will be separated with 50% efficiency. Equation 1.1 illustrates how the separated particle diameter is influenced by many factors including tangential velocity, device geometry, and particle density:

$$x_{50} = \sqrt{\frac{9 v_{rCS} \mu D_x}{\rho_p v_{\theta CS}^2}} \tag{1.1}$$

where v_{rCS} is radial velocity, μ is the fluid viscosity, D_x is the vortex finder diameter, ρ_p is the particle density, and $v_{\theta CS}$ is the tangential velocity. Highly optimized cyclones have been designed to filter particulate with diameters as small as 50 nm [6]. Cyclones have been studied as a feasible solution for maintaining air quality in manned missions to the surface of the Moon and Mars [7]. Due to the mechanisms by which cyclone separators filter out particulate matter (PM), the absence of a strong gravitational field has little effect on the operation and efficiency of the cyclone [2]. While the operating pressure affects the cyclone efficiency, the average separated diameter decreases with lower pressures. Both of these phenomena will be discussed later in this section.

While the design and operating conditions of cyclones vary greatly, there is a common, simple and robust operating mechanism throughout. All centrifugal separators work by inducing rotational flow (vortex motion) on the working fluid. While the operating fluid in this work is air, cyclones can accommodate both liquids and gases for operation. There are two common techniques for creating vortex flow in these separators. The first, and most common, is via a tangential inlet attached to a cylinder geometry. This type of separator is typically referred to as a tangential inlet cylinder-on-cone cyclone. Variations of the tangential inlet exist, including what are known as "scroll" inlets that work to introduce the flow with minimal impact [2]. There are also cyclones that have multiple equidistant tangential inlets to increase flow symmetry and stability [8]. All of these inlets have the same intention, to introduce the fluid tangentially to a cylinder to induce rotational flow. The second type of centrifugal separator is a swirl tube. Swirl tubes operate using the same rotational flow and centrifugal forces; however, the geometry and method for inducing vortex flow is different. While cyclone separators typically use tangential inlets, swirl tubes use "swirl vanes" placed inside of an axial inlet. Swirl tubes, generally, have a constant cross-section in the axial direction; meaning, rather than having a cylinder on cone geometry, a constant cylindrical shape is used throughout. Figure 1.1 illustrates the basic geometry of both a cyclone separator and a swirl tube.

In what are known as reverse-flow centrifugal separators, the fluid enters the separator and, via a vortical flow, travels down the device to the vortex end, where the flow then reverses and travels upward through the exit at the top center of the device. The vortex end in a centrifugal separator is characterized by the reversing axial velocity. The reversed axial flow traveling up the center of the device maintains a rotational component, thus creating a double vortex structure depicted in Figure 1.1. The end of the cone section is typically attached to a hopper or collection bin,

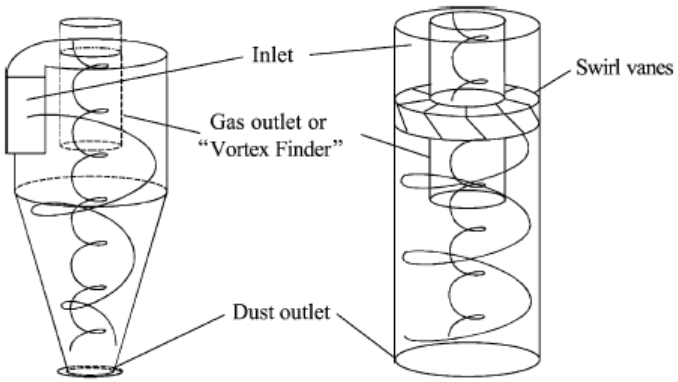

Figure 1.1: Sketch of cyclone separator and swirl tube (A. Hoffmann [1], used with permission).

to hold the captured PM. Some designs implement an underflow in this section to prevent re-entrainment of separated particulate into the main body of flow. Some swirl tube designs do not rely on the reversal of the axial velocity. Instead, two concentric tubes are used with the processed fluid exiting through the center tube and the "dirty" fluid continuing in the outside tube. This type of setup is often referred to as a "straight-through" or "uniflow" configuration [2]. Since the major velocity component of the fluid is in the tangential direction, both axial and radial velocities are considered secondary flows. The secondary axial flow is directed downward toward the cone apex at the outer wall of the cyclone. This is the mechanism by which the particles are removed from the cyclone volume. Due to flow instabilities associated with rotational flow, the particles at the wall tend to lump together in slow moving spiral waves that move down the length of the cyclone [9]. In the center of the cyclone, the axial velocity is directed up and through the vortex finder. Although the axial velocity in this inner vortex is large enough to be of consideration, a large tangential component of the velocity still exists. This swirling motion in the fluid continues well into the vortex finder and out of the system. The gradual reduction in tangential velocity due to viscosity is by far the greatest area of pressure drop in the cyclone system [2]. Some of the energy stored in the dynamic pressure component of the swirling flow can be recovered using flow "straightening" vanes; however, the static pressure of the air exiting the system will always be less than that entering. Since the pressure drop in a centrifugal separator is of critical importance in regards to the efficiency of both the cost of operation and particle separation, it will be discussed further in section 1.1.3.

1.1.2 Flow Structure

Within the cylinder and cone sections of the cyclone, there exist multiple complex flows which affect the particle separation and cyclone efficiency.While the main component of the flow is tangentially directed, axial and radial flows are found in both the inner and outer vortex flows. In the commonly used cylinder-on-cone cyclone, with a tangential inlet, the flow is accelerated after entering the system via a constriction in flow area by fluid that has already entered and circled around the device. This accelerated flow, driven by the device geometry, is then forced into a vortex flow. The swirling flow previously mentioned is comprised of two distinct regions due to the effects of viscosity; the inner or core vortex, and the outer vortex. The corresponding structure is referred to as a Rankine vortex. The two vortex regions take on very different flow regimes which result in an overall flow that is highly turbulent and unstable. A multitude of different mathematical models are available to describe this Rankine flow, with the "n-type" model being the simplest [2]. Both flow regimes follow a power law which describe the tangential velocity, and changes only slightly depending on the region of interest. First introduced by Alexander in 1949 [10] , Equation 1.2 defines the "n-type" model. Here, C is a constant, r is the spatial coordinate in the radial direction, and the exponent n varies depending on the flow regime:

$$v_\theta = \frac{C}{r^n} \tag{1.2}$$

The outer vortex, which closely resembles a free vortex flow, typically gives values for n between 0.5 and 0.8 [1]. In this outer vortex angular momentum is conserved, and thus the tangential velocity decreases moving outward from the axis of rotation. The inner vortex, which is a forced-vortex displaying solid body rotation, also follows the form of Equation 1.2; however, $n = -1$. Since angular momentum increases directly with distance from the axis of rotation, the equation for tangential velocity can be rewritten as:

$$v_\theta = \omega r \tag{1.3}$$

here, ω is the angular velocity. In the core vortex, the tangential velocity increases with radial position, reaching a maximum near the radius corresponding to the radius of the vortex finder. Here, the flow transitions into the free vortex flow described above. This combined forced- and free-vortex is typically referred to as a Rankine vortex. The mathematical explanation of the velocity field seems to show an increase in velocity (in the forced-vortex) followed by a decrease in velocity (in the free-vortex) as the distance from the axis of rotation increases. In reality, the momentum is

transported into the system at a radius corresponding to the centerline of the inlet, R_{in}. From there, the momentum is diffused via viscosity both inwards, toward the axis of rotation, and outwards, toward the outer cyclone wall. From this perspective, two free-vorticies are formed rather than the Rankine combination which more convenient for mathematical descriptions of the flow.

The radius where the forced vortex meets the free vortex can be extended into an imaginary annular surface that extends along the length of the cyclone. This "control cylinder" (CS) is the center of a second method for determining both the velocity and pressure drop within a cyclone. Proposed by Barth in 1956, this model incorporates the theory that the accelerated maximum tangential velocity in a cyclone can be determined using the inlet velocity, the wall velocity, and a ratio of angular momentum [11]. Figure 1.2 illustrates the common geometrical notation that will be used in the proceeding discussion on Barth's method.

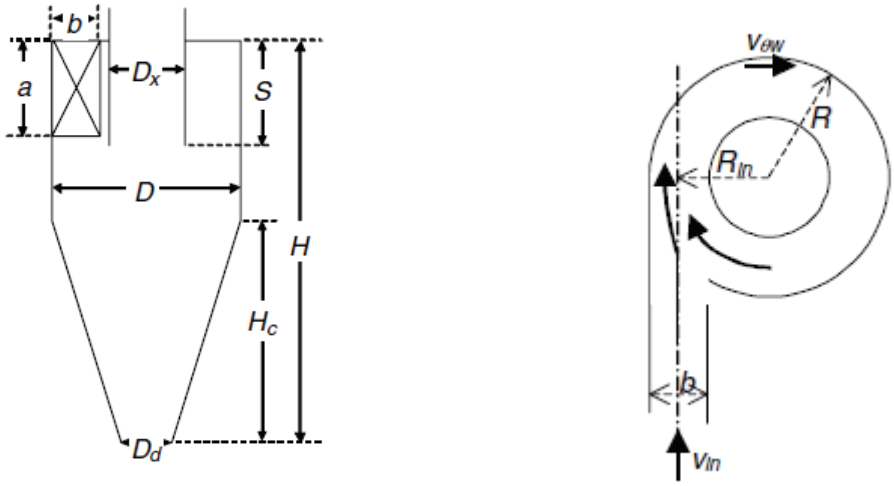

Figure 1.2: Sketch and cross section of cyclone geometrical notation (A. Hoffmann [2], used with permission).

As in Equation 1.1, D_x is the vortex finder diameter, D is the cylinder diameter, D_d is the particle-laden fluid exit diameter, a and b are the inlet height and width respectively, H is the total length of the cylinder and cone sections, and H_c is the cone length. For calculation purposes, R is defined as the cylinder radius and R_{in} is the radius corresponding to the middle of the inlet ($R_{in} = R - \frac{b}{2}$). Using the method proposed by Barth, the maximum tangential velocity is found using a non-dimensional value α:

$$\alpha = \frac{v_{in} R_{in}}{v_{\theta w} R} \tag{1.4}$$

While α was given in graphs from empirical data collected by Barth, it was later put

into a mathematical from by Muschelknautz [12, 13]. This form considers geometric parameters relating the fluid acceleration to the ratio of inlet width and cylinder radius:

$$\alpha = 1 - 0.1\left(\frac{b}{R}\right)^{0.5} \tag{1.5}$$

From Equation 1.5 one can gather that as the inlet width, b, increases, with a constant cylinder radius, R, the value of α decreases. Using this in conjunction with Equation 1.4, a connection can be made between the ratio of b to R and the acceleration of the fluid. More directly, it is evident that as α decreases, the tangential velocity at the wall, $v_{\theta w}$, increases.

As Equation 1.1 illustrates, an increase in maximum tangential velocity is ideal for particle separation. With this in mind, it should be noted that b should not be greater than the space between the vortex finder and the cylinder wall. At this point the incoming flow can directly impact the vortex finder. In clean flow this causes vibrations and stress on the vortex finder and induces a different axial flow pattern than what is typically found in the cyclone separator [14]. A typical reversed flow cylinder-on-cone separator will display an axial flow profile resembling an inverted "W"; however, if the inlet width is too large the axial profile will resemble an inverted "V" [14]. With particle-laden flow, the repercussions for an over-sized inlet can be structural damage due to the impact of particles on the vortex finder. Along with reduced service lifetime, the particle separation efficiency has been shown to decrease with increasing inlet width [14]. Since particle separation is dependent on the imbalance between the inward drag force and the outward centrifugal force, particle entrainment into the core flow causes a performance reduction. To mitigate this phenomenon, the quantity, $R - R_{in}$, should be minimized. Assuming PM enters the cyclone at R_{in}, increasing the inlet width clearly introduces particles closer to the core flow, and therefore increases the probability that the particles will not be collected.

Finally, a connection must be made between the wall tangential velocity and that at the CS. Since the flow regime in the outer vortex is accurately described as a free vortex, it can be concluded that the maximum tangential velocity at the CS increases with the wall tangential velocity, $v_{\theta w}$. However, the final velocity at the CS is not only a function of geometry, but also the friction factor, f. This friction factor draws influence from many sources, the most obvious being the wall roughness of the cyclone. Being an internal flow, cyclone vortex flow is heavily affected by wall roughness much in the same way pipe flow is affected. A rougher surface contributes to greater frictional losses at the wall, which propagate throughout the inner and outer vortex flows. Along with this common factor, frictional losses in cyclones are also affected by particulate loading. Since most of the particulate that enters the

cyclone will eventually reach the wall, the accumulation of dust and other particulate contributes to the perceived wall roughness thus increasing frictional losses [12, 13]. Equation 1.6 provides the expression for tangential velocity of the CS using Barth's method:

$$v_{\theta CS} = \frac{v_{\theta w}\left(\frac{R}{R_x}\right)}{\left(1 + \frac{H_{CS} R \pi f v_{\theta w}}{Q}\right)} \tag{1.6}$$

here, H_{CS} is the height of the control cylinder measured from the bottom of the vortex finder to where it intersects the cone, R_x is the radius of the vortex finder, and Q is the volumetric flow rate at the inlet. In Figure 1.3, one can see the CS extended from the bottom of the vortex finder to where it intersects with the cone. In Barth's derivation, the CS acted as an infinitesimal surface where all the frictional drag forces can be represented. Relative to this CS, both the inner and outer vortex structures can be modeled as free vortex flow.

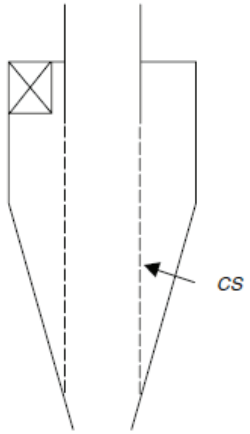

Figure 1.3: Sketch of Barth's control surface (A. Hoffmann [2], used with permission).

To establish a relationship for the friction factor, f, a special *cyclone Reynolds number* must be defined. Equation 1.7 shows the cyclone Reynolds number as defined by Muschelknautz [15], who found that for a cyclone Reynolds number greater than 400, f is approximately constant only showing a dependency on the relative wall roughness.

$$Re_{cyc} = \frac{Re_x}{4\frac{H}{D_x}\left(\frac{D}{D_x} - 1\right)} \tag{1.7}$$

Table 1.1: Friction coefficient values from relative roughness.

$\frac{h}{R}$	f_{air}
Hydraulically Smooth	0.005
$1 \times (10^{-3})$	0.010
$6 \times (10^{-3})$	0.025

where,

$$Re_x = \frac{\rho v_x D_x}{\mu} \tag{1.8}$$

is the Reynolds number of the exiting flow in the vortex finder, with v_x the average velocity through it. The relative roughness is given by the typical ratio $\frac{h}{R}$, which is given with respect to the cylinder radius rather than the diameter commonly used in pipe flow applications. This relationship accounts for the surface friction factor in regards to clean flow, or flow where no particulate is introduced. To distinguish between the two friction factors, f_{air} will be used for clean air and f_{dust} will be used to account for particle loading. Above the critical cyclone Reynolds number, the values for f_{air} can be found in Table 1.1 [15].

To account for the additional friction factor associated with particle loading, Muschelknautz defined f_{dust} using a mass ratio loading factor given by, c_o. Equation 1.9 displays the relationship between c_o and f_{dust}. The total friction factor, f, is simply a sum of the two previously defined factors, f_{air} and f_{dust}.

$$f_{dust} = 0.015(c_o)^{0.5} \tag{1.9}$$

A multitude of over numerical methods exist attempting to characterize the complex vortex flow inside of the cyclone separator. One more worth reviewing in detail is that established by Meissner and Löffler in 1978 [16]. Similarly to Barth's method, the Meissner/ Löffler method utilized a balance of forces to determine the fluid tangential velocity. Rather than examining a force balance on a particle at a control surface, this method considers the angular momentum entering and exiting a cylindrical control volume. Since angular momentum is the moment-of-momentum, this convective angular momentum term is balanced with the moments produced by the frictional forces acting on the top and bottom control surfaces. Figure 1.4 illustrates the differential cylinder utilized in this method.

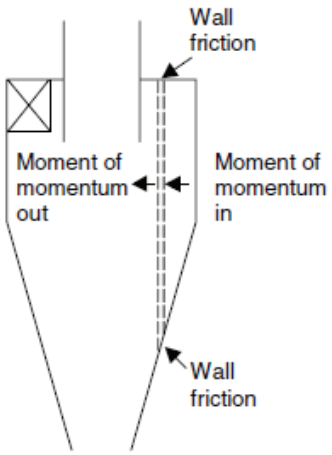

Figure 1.4: Sketch of control volume used in the Meissner and Löffler method (A. Hoffmann [2], used with permission).

Like Barth's method the flow acceleration due to inlet contraction is established as a geometric parameter, this time denoted by β. Equation 1.10 defines the geometric value with a relationship between the inlet width and cyclone barrel radius, much like that in the Barth method:

$$\beta = -0.204\frac{b}{R} + 0.889 \tag{1.10}$$

$$v^*_{\theta w} = \frac{v_{in}}{\beta} \tag{1.11}$$

Using this acceleration factor, the accelerated tangential velocity is simply given by dividing the inlet velocity, v_{in}, by β given in Equation 1.11. The asterisk denotes a *modified* tangential velocity. To find the tangential velocity, the frictional effects on the cylinder walls must be considered. Equation 1.12 displays the relationship between the *modified* tangential velocity and the reduced tangential velocity.

$$v_{\theta w} = \frac{\bar{v_z}}{f_{cyl}H^*_{cyl}}\left[\sqrt{\frac{1}{4} + f_{cyl}H^*_{cyl}\frac{v^*_{\theta w}}{\bar{v_z}}} - \frac{1}{2}\right] \tag{1.12}$$

In Equation 1.12 $\bar{v_z}$ is the mean axial velocity inside the cyclone given by Equation 1.13. f_{cyl} is a friction factor used to model the frictional losses between the fluid and the cylinder walls. Initially, the losses at the cylindrical, conical, and top walls were all defined with their own respective subscripts; however, Mothes and Löffler (1988) later showed that they could all be the equal being somewhere between 0.0065 and 0.0075 [17]. H^*_{cyl} is given in Equation 1.14 as a function of the inlet dimensions and cylinder radius and height:

$$\bar{v_z} = \frac{4Q}{\pi D^2} \tag{1.13}$$

$$H^*_{cyl} = \frac{a}{R}\left[\frac{-arcos(1-\frac{b}{R})}{2\pi}\right] + \frac{H_{cyl}}{R} \tag{1.14}$$

Finally, the tangential velocity can be defined as a function of radial position, reduced wall tangential velocity, wall friction factors, mean axial velocity, and the angle between cyclone axis and the cone wall. Equation 1.15 differentiates the friction factors with subscripts to stay with the original definitions. The angle between the cyclone axis and the cone wall is denoted by γ.

$$v_\theta(r) = v_{\theta w}\left\{\frac{r}{R}\left[1 + \frac{v_{\theta w}}{\bar{v_z}}\left(f_{lid} + \frac{f_{cone}}{sin\gamma}\right)\left(1 - \frac{r}{R}\right)\right]\right\}^{-1} \tag{1.15}$$

While the Meissner and Löffler method provides a the tangential velocity as a function of radial position rather than relying on the assumption of loss-free flow like the "n-type" and Barth models, it cannot account for the effects of mass loading. In this regard the modified Barth method proposed by Muschelknautz provides an advantage. It also only applies to the cylinder-on-cone separator design with a tangential slot inlet and thus will not work in swirl tube analysis.

Other mathematical models have been developed in attempts to accurately represent the flow field inside a cyclone separator. Most are based on modifications to the methods presented above or are setup in a manner to solve numerically. While these other models work to define the flow field, the models presented above have proven to yield accurate results for the purpose of both experimentation and commercial cyclone design. For this reason, only a brief review of other methods will be provided.

A combined theoretical and experimental approach was utilized by Reydon and Gauvin (1981) to produce two simple expressions for tangential velocity [18]. In this method the tangential flow is split into the forced vortex and loss-free vortex discussed above. Using this as a base, empirical coefficients were obtained from regression analysis. Equation 1.16 and 1.17 clearly show the "n-type" model inspiration of a forced- and free- vortex, respectively:

$$v_\theta = 1.35 v_{in} r \mathrm{e}^{-0.153 v_{in}^{-0.17} r} \tag{1.16}$$

$$v_\theta = \frac{14.79 v_{in}}{r^{0.72}} \tag{1.17}$$

Ogawa suggested a more complex method for calculating the flow field within a cyclone separator largely based on coefficients K_0 and n [19, 20]. Both of these coefficients are functions of the Reynolds number and the cyclone geometry.

Ingham and Ma proposed a method by which the the Navier-Stokes equations can be simplified and solved numerically. Previous theoretical particle collection studies by Bloor and Ingham [21–23] showed good agreement with experimental studies performed by Kelsall [24]. In these works an assumption of axisymmetry allowed for streamline functions to be established. Assuming the flow is inviscid then provides equations for axial and radial velocity profiles. Since the effects of viscosity affect the tangential velocity profile, either the power law suggested by Svarovsky [25], which is essentially the power law profile given in Equation 1.2, or an approximation proposed by Bloor and Inham can be used. The approximate differential equation solutions given by Bloor and Ingham assume tangential velocity is only a function of radial position thus allowing for the Navier-Stokes equations to be simplified and solved numerically. This model was then used to along with a spatially discretized grid and a k-ϵ renormalization group (RNG) turbulence model to solve for a flow field, pressure drop, and collection efficiency [26]. The advantages and disadvantages of various computational models, which include the k-ϵ RNG model, will be discussed further in a later section.

Up until this point the focus has been placed on accurately describing the tangential velocity profile within the system. While this is the major component of the flow field and is critical to the efficiency of the cyclone, a few other items must be discussed to completely describe the character of the flow within the system. The most common way to characterize fluid motion is with the Reynolds number which has already been introduced in Equation 1.8. This, however, is the Reynolds number describing the flow exiting the system via the vortex finder. Similarly, to give insight into the swirling flow within the barrel and cone sections of the cyclone, the Reynolds number can be defined using the inlet velocity, v_{in}, and the barrel diameter, D as the length scale. This form of the Reynolds number, shown in Equation 1.18, will be used throughout this work.

$$Re = \frac{\rho v_{in} D}{\mu} \tag{1.18}$$

Most cyclones operate well above what would be considered the *critical* Reynolds number. A study by Overcamp and Scarlett in 1993 [27] showed that the particle separation efficiency in cyclones is relatively constant when $Re > 2 \times 10^4$. Particle separation is often characterized using the Stokes number, Sk. When characterizing a centrifugal separator based on particle separation, a cut-off size associated with the particle diameter that will be collected 50% of the time is denoted by x_{50}. Since the Stokes number, given in Equation 1.19, includes the particle diameter, one can determine the Stokes number for the cut size of a given cyclone. This can then be used as a metric for cyclone scaling and similitude [2]. It was this Stokes number

corresponding to the 50% cut size that Overcamp and Scarlett showed was relatively constant above the *critical* Reynolds number.

$$Sk = \frac{\Delta \rho x^2 v_{in}}{18 \mu D} \tag{1.19}$$

The swirling flow in centrifugal separators can also be characterized using the swirl number. Typically, the swirl number is a representation of the ratio of axial flux of angular momentum and the axial flux of axial momentum. However, since the flow in cyclones is in both axial directions a "geometric" swirl number was proposed by Gupta in 1984 [28]. Equation 1.20 displays the geometric swirl number as defined by Gupta.

$$S_g = \frac{\pi D_x D}{4 A_{in}} \tag{1.20}$$

A common byproduct of swirling flows is instability, and the flow inside of a centrifugal separator is no exception. An initial analysis using the Rayleigh criterion of a two-dimensional inviscid flow gives a first approximation that the vortex flow in a cyclone is stable [29–31]. This method works by considering the energy change associated with the radial exchange of two differential fluid volumes. If the two elements are located at r_1 and r_2, with $r_2 > r_1$, then the Rayleigh stability criteria are:

$$\rho_1 \omega_1 r_1 < \rho_2 \omega_2 r_2 \qquad \text{Stable} \tag{1.21}$$

$$\rho_1 \omega_1 r_1 = \rho_2 \omega_2 r_2 \qquad \text{Neutrally Stable} \tag{1.22}$$

$$\rho_1 \omega_1 r_1 > \rho_2 \omega_2 r_2 \qquad \text{Unstable} \tag{1.23}$$

here, a "stable" flow will dissipate a perturbation, while a "neutrally stable" flow will allow a perturbation to continue without an increase or decrease in the magnitude. An "unstable" flow will allow the magnitude of a small perturbation to increase. The inner, forced vortex, and the outer, free vortex, correspond to the first two criteria respectively giving a "stable" flow. The last criterion corresponds to an energy release associated with the radial exchange that would cause the instability to grow. However, the flow inside a cyclone separator is three-dimensional and viscous forces can lead to larger low frequency instabilities. This low frequency oscillation manifests itself in the vortex core of the flow. First observed by Smith using smoke tracers and strobe lights [32], the precessing vortex core (PVC) has been of great interest in cyclone studies. The PVC has also been visually studied by Chanaud in a hydroclone [29]. Ito et al. [33] showed that the frequency at which the vortex core precessed was linearly related to the inlet flow rate of the cyclone. Sloan et

al. [30] found the frequency of cyclone core precession to fall between ten and 200 Hz. One can characterize the PVC by comparing the timescale of unsteady precession fluctuations to the convective timescale of the mean flow. This is described by the Strouhal number given in Equation 1.24.

$$St = f_{PVC}\frac{D}{v_{in}} \tag{1.24}$$

While the process by which the precessing vortex core occurs is still not completely understood, it has been attributed to being a byproduct of vortex breakdown [29]. For example, Lopez published a series of papers studying vortex breakdown in confined cylindrical flow, finding that the mechanism of vortex breakdown is the cause of low-frequency waves traveling axially along the vortex core [34–36]. This was accomplished using non-linear dynamic theory of systems and utilizing a Hamiltonian approach to describe the system. The stability of the vortex core subjected to vortex breakdown has been studied using Hopf bifurcation by Gelfgat [37]. The PVC and the associated breakdown have also been investigated using numerical methods by Derksen [38] and Jochmann [39] respectively.

The pressure field in centrifugal separators is not nearly as complicated to understand as the velocity field. Since the greatest component of the total velocity is in the tangential direction, the pressure distribution is dominated by this flow. The relationship between tangential velocity and pressure can easily be determined by looking at the Navier-Stokes equations, and making a few simplifying assumptions. Equations 1.25, 1.26, and 1.27 are the Navier-Stokes equations of motion in cylindrical coordinates — r, θ, z — for an incompressible fluid:

$$\rho\left[\frac{Du_r}{Dt} - \frac{u_\theta^2}{r}\right] = -\frac{\partial p}{\partial r} + f_r + \mu\left[\nabla^2 u_r - \frac{u_r}{r^2} - \frac{2}{r^2}\frac{\partial u_\theta}{\partial \theta}\right] \tag{1.25}$$

$$\rho\left[\frac{Du_\theta}{Dt} - \frac{u_\theta u_r}{r}\right] = -\frac{1}{r}\frac{\partial p}{\partial \theta} + f_\theta + \mu\left[\nabla^2 u_\theta - \frac{u_\theta}{r^2} + \frac{2}{r^2}\frac{\partial u_r}{\partial \theta}\right] \tag{1.26}$$

$$\rho\frac{Du_z}{Dt} = -\frac{\partial p}{\partial z} + f_z + \mu\nabla^2 u_z \tag{1.27}$$

here, D indicates the material derivative, and ∇^2 is the Laplacian. Now, assuming the flow is inviscid, axisymmetric, purely azimuthal, and in the absence of any external body forces, the equations of motion are greatly simplified. The relationship between tangential velocity and pressure immediately presents itself in Equations 1.28, 1.29, and 1.30:

$$\rho\frac{u_\theta^2}{r} = \frac{\partial p}{\partial r} \tag{1.28}$$

$$\frac{\partial u_\theta}{\partial t} = 0 \tag{1.29}$$

$$\frac{\partial p}{\partial z} = 0 \tag{1.30}$$

Equation 1.28 shows that the radial pressure gradient is only a function of tangential velocity, while Equation 1.30 leads to the conclusion that there is no pressure gradient in the z direction. Together, these two equations give concentric cylinders of increasing pressure as the distance from the axis increases. Equation 1.29 illustrates that if the flow is purely azimuthal and axisymmetric, it must also be steady. Since the tangential velocity of the flow field within the cyclone is a function of radial position, as shown earlier in this section, for a steady flow the pressure will also solely be a function of r.

1.1.3 Pressure Drop

One of the values by which cyclone performance is measured, the cut size x_{50}, was discussed briefly in Section 1.1.2. This parameter is critically important when determining the applications for which a cyclone is suitable. As shown in Equation 1.1, this average particle diameter which will be separated out of the flow in a cyclone is affected by a variety of variables: maximum tangential velocity, particle density, and the cyclone geometry. From Equation 1.1 one can see that simply increasing the maximum tangential velocity will lower the cut size diameter and thus make the cyclone "more efficient". However, in the same way modifying the inlet dimensions yielded certain advantages and disadvantages, increasing the azimuthal velocity inside the cyclone generates losses that are not immediately apparent.

As with any internal flow, the pressure drop across devices implemented into the system greatly affects the cost of operation. The centrifugal separator is no exception. A certain *inlet pressure* drives the flow into the device, and, after making several revolutions around the cyclone, the fluid exits with a lower *exit pressure*. Many different factors contribute to the pressure loss across a cyclone separator, with the greatest being the very swirling motion that allows the device to operate. The pressure drop can in fact be separated into four different partial pressure drops [40]. The first pressure drop occurs when the gas expands as it enters the cyclone. The second and third pressure drops are caused by the swirling motion inside the cyclone body, and the frictional losses along the cyclone walls. The final pressure drop, which is the greatest, occurs in the vortex finder as the fluid is exiting the system. This major pressure loss is due to the swirling motion that persists in the fluid flow as it exits via the vortex finder, and is greatly dependent on the maximum tangential velocity [2, 14]. The pressure drop within the vortex finder is so great due to the

inability to recover the energy imparted on the flow to produce the swirling motion. In the absence of any flow-straightening devices, the rotational component of the flow will persist until viscous effects slowly dissipate the momentum in that direction. Flow-straightening vanes can be placed in the exit tube; however, even with these efficient energy recovering devices, major pressure losses still accrue. The geometry of the cyclone also impacts the pressure drop of the entire system. Increasing the inlet height or increasing the diameter of the vortex finder both have a negative correlation with the total pressure drop. While increasing the length of the vortex finder has a positive correlation on the pressure drop [14, 40].

Some empirical models have been developed to calculate the pressure drop across a cyclone separator. While these methods do not attempt to capture all of the physical phenomena occurring during operation, the results are often accurate enough to influence engineering decisions. One such model is that developed by Shepherd and Lapple (1940) [41]. This model resembles the more typical head loss model used in piping calculations. First, a head loss coefficient is calculated using a ratio of the inlet and exit diameters, along with a constant, K:

$$H_v = K\frac{ab}{D_x^2} \tag{1.31}$$

where K ranges from 12 to 18 [42]. Then the head loss coefficient is multiplied by the kinetic term to give the total pressure drop from inlet to outlet:

$$\Delta p = \frac{1}{2}\rho_g v_{in}^2 H_v \tag{1.32}$$

In Equation 1.31, K is typically set to 16, which gives a satisfactory levels of accuracy for engineering calculations [42]

Other, more detailed, models were proposed by both Stairmand (1949) [43] and by Barth (1956) [11]. Both of these methods are based on calculating the dissipative losses in the system. The Stairmand method is accomplished by first considering an angular momentum balance, then deriving an estimate for pressure losses at the entrance and exit, along with those lost in the static pressure of the swirling flow. A nondimensional form of the pressure drop can be described using the Euler number given as:

$$Eu_{in} = \frac{\Delta p}{\frac{1}{2}\rho v_{in}^2} \tag{1.33}$$

In the context of the Stairmand pressure drop model, the Euler number can also be defined as:

$$Eu_{in} = 1 + 2q^2\left(\frac{2(D-b)}{D_x} - 1\right) + 2\left(\frac{4ab}{\pi D_x^2}\right)^2 \tag{1.34}$$

here, q is defined as:

$$q = \frac{-\left(\frac{D_x}{2(D-b)}\right)^{0.5} + \left(\frac{D_x}{2(D-b)} + \frac{4A_rG}{ab}\right)^{0.5}}{\left(\frac{2A_rG}{ab}\right)} \tag{1.35}$$

where A_r is the total internal surface area of the cyclone, and $G = \frac{f}{2}$ for which $f = 0.005$ under normal operating conditions [43]. The Barth method for calculating pressure drop is separated into two different calculations. The first of which calculating the pressure drop due to viscous effects in the body flow. The second calculation accounts for the losses found in the vortex finder. Losses at the inlet were not accounted for since they can be eliminated with careful design of the cyclone inlet. Again, the pressure drop is represented using the Euler number; however, a slightly different form is utilized giving:

$$Eu_{body} = \frac{\Delta p_{body}}{\frac{1}{2}\rho v_x^2} = \frac{D_x}{D}\left[\frac{1}{\left(\frac{v_x}{v_{\theta CS}} - \frac{(H-S)}{0.5D_x}f\right)^2} - \left(\frac{v_{\theta CS}}{v_x}\right)^2\right] \tag{1.36}$$

here, f is calculated using the method by which it was done in the Barth/ Muschelknautz velocity field formulation (using Table 1.1 and Equation 1.9). To calculate the pressure loss due to swirling flow in the vortex finder, two ratios of tangential to axial velocity are considered along with a constant K. Again, the Euler number takes a slightly different form for the flow in the exit tube:

$$Eu_x = \frac{\Delta p_x}{\frac{1}{2}\rho v_x^2} = \left(\frac{v_{\theta CS}}{v_x}\right)^2 + K\left(\frac{v_{\theta CS}}{v_x}\right)^{\frac{4}{3}} \tag{1.37}$$

using $K = 3.41$ or 4.4 for vortex finders with either a round or sharp edge respectively. In the Barth pressure drop model, one can see that the tangential velocity at the CS must be calculated in order to perform the pressure drop calculations. This comes from the derivation of the body pressure drop based on frictional losses at the CS typical to Barth formulations.

Finally, a truly theoretical pressure drop model can be developed based on the flow physics of the core vortex. The core vortex, with axial flow up through the vortex finder, is assumed to maintain a Rankine vortex flow, similar to that in the larger cyclone body. For derivation purposes, this flow is assumed to be inviscid,

axisymmetric potential flow. In the "outer" free-vortex, potential flow theory gives a constant axial velocity, while in the "inner" forced-vortex the axial velocity is negligible. In this model a stationary, low pressure core is formed due to the swirling motion of the fluid. This core forms a cylinder of constant diameter which spans the length of the cyclone. The surface corresponding to the radius of this core, R_s, is most easily imagined using a hydrodynamic analogy developed by Smith, Jr. [32].

If the cyclone is completely void of water when it starts, the water will enter the device and begin swirling around and filling up the volume of the cyclone. As it swirls, an "air-core" will form in the center along the central axis of the cyclone. As more water enters the cyclone the diameter of the core will decrease, eventually reaching the diameter of the vortex finder, D_x. At this point, the water, still in a swirling motion, will begin to "climb" the interior wall of the vortex finder moving towards the exit. Once the cyclone is operating at steady-state, there will be an "air-core" along the central axis of the cyclone extending from the bottom of the cone to the vortex finder exit. In this analogy the low-pressure core is easily imagined due to the difference in density between air and water; however, in both a hydroclone and a normal cyclone, the formation of said core is caused by differences in angular momentum. In the central core of the flow, there is a constant pressure, p_{out}, which exerts a force on the core surface. The difference between p_{out} and the inlet pressure, p_{in}, will be used to determine the pressure drop across the cyclone in this model.

The radius of the low-pressure core is a function of the flow rate and the annular thickness of the flow inside the vortex finder. In order for the flow to reach equilibrium, the thickness of the flow in the vortex finder must be enough to maximize the volumetric flow rate. Smith draws a helpful analogy to the two-dimensional, open-channel flow over a broad-crested weir. In this example, the depth of the fluid is set such that the volumetric flow over the weir is maximized. This corresponds to the critical depth of the flow. Again, in this example, the free surface of the water is set by a discontinuity in density; the "free surface" in the cyclone is set by a discontinuity of angular momentum.

To start the mathematical derivation of this pressure drop model, Bernoulli's equation is implemented:

$$\frac{v_r^2}{2} + \frac{v_\theta^2}{2} + \frac{v_z^2}{2} + \frac{p_2}{\rho} = \frac{p_1}{\rho} \tag{1.38}$$

Assuming the radial velocity is negligible, Equation 1.38 can be rearranged to solve for the axial velocity. Here, Γ will be used to signify the angular momentum such that the substitution $v_\theta r = \Gamma$ can be made to abide by the original formulation put forth by Smith. Partially solving for v_z and substituting in Γ, Equation 1.38 becomes:

$$v_z^2 = \frac{2\Delta p}{\rho} - \frac{\Gamma^2}{R_s} \tag{1.39}$$

where $\Delta p = p_1 - p_2$. At this point it is helpful to define the volumetric flow rate in terms of the axial velocity in the annular flow through the vortex finder:

$$Q = \pi(R_x^2 - R_s^2)\sqrt{\frac{2\Delta p}{\rho} - \frac{\Gamma^2}{R_s}} \tag{1.40}$$

where the second term on the right-hand-side of the Equation 1.40 is the axial velocity from Equation 1.39. As stated previously, at steady-state, the flow through the vortex finder is optimized such that the volumetric flow rate is at a maximum with respect to the radius of the low-pressure core. This requires that:

$$\frac{\partial Q}{\partial R_s} = 0 \tag{1.41}$$

After simplifying, the term R_s is replaced by R_{cr} to indicate that it is the critical radius corresponding to maximum volumetric flow rate:

$$\frac{R_{cr}^2 v_z^2}{\Gamma^2} = \frac{1}{2}\left(\frac{R_x^2}{R_{cr}^2} - 1\right) \tag{1.42}$$

Since Equation 1.42 does not give an explicit relation between the axial velocity, tangential velocity, and the critical core radius established in the vortex finder, Smith produced a relationship between the nondimensionalized core radius and the volumetric flow rate. While this method works, Hoffman and Stein present an approximate equation in [2] that gives the core radius within 1% error:

$$R_{cr} = R_x\left[\frac{0.0219(v_{\theta CS}/v_x)^{-0.686} + 1}{0.700(v_{\theta CS}/v_x)^{-0.686} + 1}\right] \tag{1.43}$$

The use of v_x rather than v_z should be noted here. While both terms represent the flow through the vortex finder, v_z is purely the axial velocity, while v_x is the average velocity exiting the vortex finder. This value is used since the average velocity is often measured during experimentation rather than a single component of the velocity. To finally find the pressure drop in the core flow model, Equation 1.39 is substituted into Equation 1.42 giving:

$$\Delta p = \frac{\Gamma^2\rho}{2R_{cr}^2}\left[\frac{1}{2}\left(\frac{R_x^2}{R_{cr}^2} - 1\right) + 1\right] \tag{1.44}$$

which can then be expressed in terms of the Euler number by diving by the kinetic energy per unit volume:

$$Eu = \frac{\Delta p}{\rho \frac{v_x^2}{2}} = \frac{\Gamma^2}{v_x^2 R_{cr}^2}\left(\frac{R_x^2}{2R_{cr}^2} + \frac{1}{2}\right) \tag{1.45}$$

Since the pressure drop in this model is derived assuming the flow in vortex finder is a free-vortex, the term Γ is constant, and thus can be calculated using any known tangential velocity and corresponding radius. In the context of this work, $v_{\theta CS}$ should be used with R_x since methods to calculate these quantities have already been reviewed in Section 1.1.2.

1.2 Pressure Sensitive Paint

Measuring the flow field within the cyclone separator is a challenging process for a multitude of reasons. The high degree of turbulence in the flow field renders standard mean flow measurement techniques, such as pitot-static tubes and hot-wire anemometers, inaccurate. Moreover, placing measurement devices into the flow can produce disturbances artificially altering the flow field. Additionally, measurements of internal flows present unique problems arising from placing the measurement device without creating leaks in the system.

Noninvasive measurement techniques, such as Laser Doppler Anemometry (LDA), can be used to take measurements without disturbing the flow field. This method requires the flow to be seeded with tracer particles from which the laser light is reflected. As the name suggests, the velocity is then calculated using the Doppler shift caused by the particle either moving towards, or away from the light sensor. While this measurement technique solves some problems it creates others. The introduction of seeder particles into a flow can affect the overall flow, as was highlighted in the Muschelknautz calculation of the velocity field discussed in Section 1.1.2. As a result, measurements collected with this technique describe the a particle laden flow through a device rather than that of a "clean" flow. Certain assumptions are also made to acquire LDA measurements; one of them being that the seeder particle follows the flow exactly. This can be a problem with a device such as the cyclone separator, which is designed to separate particles from the true path of the fluid.

To circumnavigate the issues presented above, pressure sensitive paint (PSP) has been employed for the measurement campaign presented in this work. Like Laser Doppler Anemometry, measurements taken with PSP do not affect the flow field within the cyclone separator. Pressure sensitive paint requires three basic components for operation: a layer of binder that acts as a base coat for the system, a luminescent particle known as luminophore, and a light source to illuminate and excite the luminophore. The luminophore molecules are excited with the light source into an energy level above the ground state. At this point, there are few mechanisms

by which the molecule can dispel the gained energy to revert back to the ground state. The two mechanisms that are of critical importance in PSP measurements are luminescence and oxygen quenching. Through luminescence the molecule releases energy by emitting a photon of a slighter longer wavelength than that which was absorbed by the light source; this is known as Stokes-shifted luminescence [44]. Oxygen quenching occurs when an oxygen molecule collides with an excited luminophore molecule thus transferring the energy to the oxygen molecule. The function of PSP is then based on the balance between these two main methods of energy dissipation. Higher localized pressures are associated with greater partial pressures of oxygen, which leads to a greater probability of collision between the oxygen and luminophore molecules. A third method through which energy is dissipated is thermal deactivation [44]. The process of thermal deactivation leads to drops in luminescent intensity rendering it a source of error for PSP. However, this can be corrected using *in-situ* calibration with pressure taps in the test specimen.

The binder layer mainly acts as a surface on which the luminescent particles attach. Although the binder itself does not have any luminescent properties, the composition of said layer can greatly affect the performance of the PSP. The most influential of binder characteristics is porosity. Since the pressure measuring mechanism is the oxygen quenching of excited luminophore molecules, the response rate of of PSP is directly related to oxygen diffusion through the binder. From a modeling perspective, oxygen diffusion into the base layer can be modeled using the one-dimensional, unsteady diffusion equation with a boundary condition allowing zero flux at the wall [44]. Solutions of this form have been given by Carroll et al. [45], Mosharov et al. [46], Winslow et al. [47], Liu and Sullivan [48], and Gregory and Sullivan [49]. Using this formulation, based on the binder layer thickness, a homogeneous polymer PSP — one in which the luminophore and binder are mixed together as one solution — has a diffusion time scale of approximately 0.1 seconds [44]. This, being an indicator of measurement response times, is obviously too long to resolve most temporal pressure fluctuations.

To decrease the diffusion timescale, porous binders were developed to increase the air-luminophore contact interface. Doing so reduced the diffusion timescale to microseconds, which could accurately resolve high frequency fluctuations. The implementation of porous binders in pressure sensitive paints has been accomplished by a few different methods including: thin-layer chromatography (TLC), Anodized aluminum, and polymer/ceramic mixtures. TLC allows for easy application of the luminophore as the model can be dipped into the solution, which provides sufficient coverage and cohesion. However, this method produces brittle samples which then limit the range of geometries with which the process is suitable [44].

Using anodized aluminum as the base for PSPs allows for uniform distribution

of pores in which the luminophore can attach. The process requires the aluminum to first be anodized, followed by the application of phosphoric acid onto the surface to promote absorption. The luminophore molecules are then introduced, most often, by dipping the sample in a luminophore solution. Sakaue [50, 51] and Gregory [52] provide a detailed overview of this type of application process. It has been shown that there are multiple parameters which affect the luminescence, pressure sensitivity, and temperature sensitivity [53–57]. These parameters include the polarity index of the solvent, luminophore concentration, and the duration in which the part in submerged in the solution.

The third method by which a porous binder layer can be produced is with a polymer/ceramic solution. This method allows for a wide range of geometries and materials to be used in conjunction with PSP. While the first two methods discussed above are sufficient for producing a sample coated in PSP for fast response analysis; the shape, and most importantly the material, from which the test specimens are produced limit the feasible applications for those PSPs. Polymer/ceramic pressure sensitive paints (PC-PSP) can be sprayed onto the test specimen allowing for the geometry to take on a wider array of forms and materials. The application of PC-PSP was first done by Scroggin [58] via a tape casting method. Gregory further expanded the applications for PC-PSP by developing a method to spray the base coat onto the sample [59]. The polymer/ceramic solution is created by mixing approximately 3.5% polymer, by weight, into the ceramic solution immediately before spray application to the test sample. After the base coat is applied, the luminophore can be applied via submersion into a luminophore solution or by spray application directly onto the test geometry.

The luminophore solution used in most pressure sensitive paints is typically bathophen ruthenium or Pt(II) meso-tetrakis(pentafluorophenyl)porphine, which will henceforth be referred to as PtTFPP or platinum porphyrin. Bathophen ruthenium is often used for the short lifetime of luminescence; however, it only has a pressure sensitivity of -0.2% per kilopascal on average [44]. PtTFPP has a slightly longer luminescent lifetime, but with a pressure sensitivity of -0.82% per kilopascal it is desirable for use in fast-response pressure sensitive paints where the signal-to-noise ratio (SNR) of each image is critical. For this work PtTFPP is used as the luminophore molecule.

As stated before, the luminophore molecules act by first absorbing a specific wavelength of light from a controlled source thus raising the energy of the molecule to that of an excited state, then dissipating this energy by either luminescence or oxygen quenching. PtTFPP has three bands from which it can enter an excited state with 392 nm having the highest absorption rate [60, 61]. The two other wavelengths which can be absorbed by the molecule are at 506 and 538 nm. After the molecule has absorbed the energy from one of the wavelength bands previously mentioned, the

luminescence process can begin.

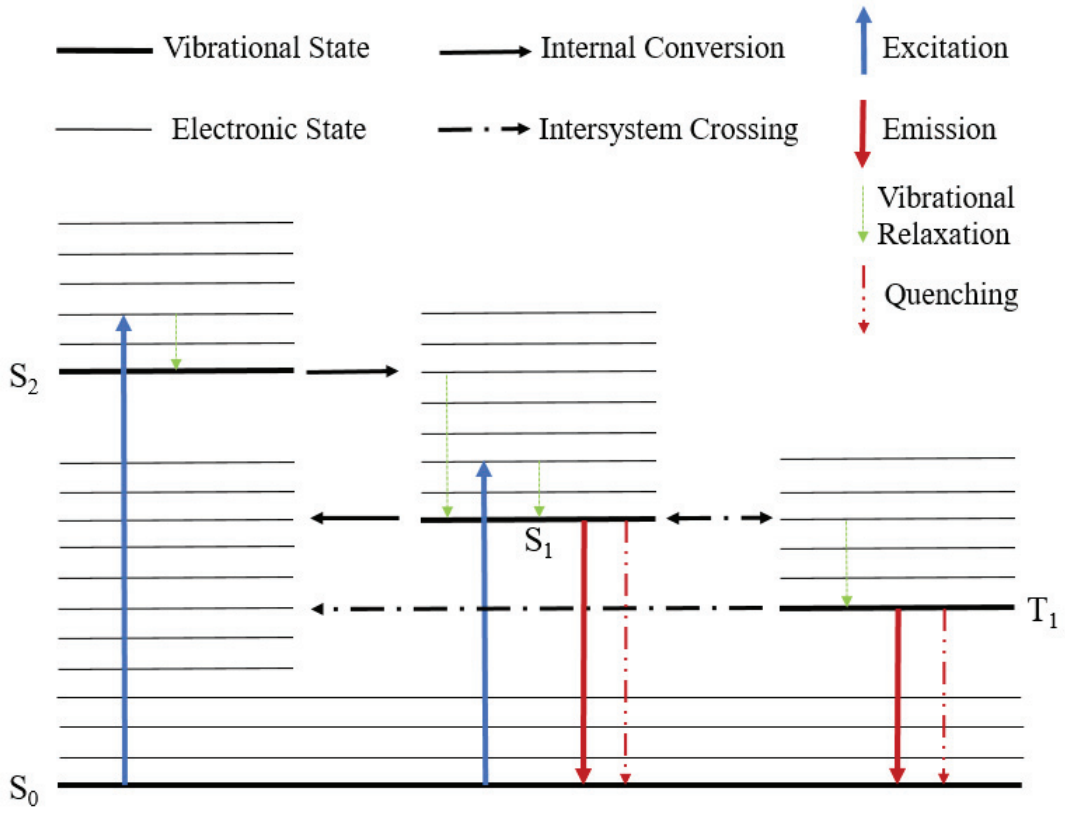

Figure 1.5: Jablonski energy level diagram showing typical luminescent process (Adapted from [3]).

If the incident light is at the 392 nm wavelength, the molecule will be excited to the S_2 singlet electronic state. If the incident light is of either of the other two wavelengths, the molecule will be excited to an S_1 singlet electronic state [3]. From this point, the luminescent dissipation of energy can proceed a number of different ways which are best described with the aid of the Jablonski diagram shown in Figure 1.5. After exciting to the S_2 electrical state, the molecule can be in any number of vibrational modes. A subsequent vibrational relaxation then occurs where the molecule will dissipate thermal energy to nearby molecules in order to "relax" to the lowest energy vibrational mode in the S_2 electronic state. At this point an internal conversion from $S_2 \rightarrow S_1$ occurs. Through thermal energy dissipation, the molecule, again, goes through vibrational relaxation to the lowest energy vibrational mode of the S_1 electronic state. The energy dissipation can now be accomplished by: fluorescence, which is the emission of radiation from a singlet state; a collision with a nearby oxygen molecule causing oxygen quenching; internal conversion to the S_0 ground state, which is followed by vibrational relaxation to the true ground state; or an intersystem crossing to a triplet state, T_1. If fluorescence occurs, the wavelength of the emitted

photon is longer than that of the incident radiation due to the thermal dissipation of energy associated with vibrational relaxation; this is known as a Stokes shift. If an intersystem crossing occurs into the T_1 triplet state, then four additional paths to the ground state are possible. Phosphorescence can occur, which is the emission of radiation from a triplet state; oxygen quenching (from $T_1 \rightarrow S_0$) state is possible; an internal conversion to an "excited" vibrational mode of the S_0 state can occur, which is then followed by vibrational relaxation; or an intersystem crossing back to the S_1 state can occur, although this needs to be thermally activated due to the energy difference between the lowest $T_1 \rightarrow S_1$ states. If the molecule crossed back to the S_1 state, the process repeats until the molecule has reached the lowest vibrational mode of the S_0 state.

The distinction between fluorescence and phosphorescence comes from different electron spin orientations, which also create the distinction between singlet and triplet states. Any of the intersystem crossing processes — $T_1 \Leftrightarrow S_1$ or phosphorescence, which itself is a radiative intersystem crossing from $T_1 \rightarrow S_0$ — are "forbidden" since the spin orientation of the electron needs to change. However, spin-orbital coupling mixes what are normally "pure" states, which in turn allows for these intersystem crossings to occur [3]. Since this is "forbidden", and requires a mixing of states, the phosphorescence process typically takes much longer and is less likely to occur by several orders of magnitude [62]. In summary, radiative emission from a singlet state transpires over an extremely short period of time and is referred to as fluorescence, while emission from a triplet state is statistically much less likely to occur, happens over a longer period of time, and is referred to as phosphorescence. The combination of both fluorescence and phosphorescence is luminescence.

The oxygen quenching process is simply the exchange of energy through a collision between a ground state oxygen molecule and an excited luminophore molecule. This phenomenon is allowed physically because the two lowest level excited states for oxygen are both singlet states. In terms of energy, both singlet states are only 1.0 eV above that of the triplet ground state [3]. Once the oxygen molecule has absorbed the energy required to jump to one of the excited states, it typically dissipates the energy through long wavelength luminescence. These radiative emissions from excited oxygen molecules typically have wavelengths greater than 1230 nm. Once the oxygen is in one of the singlet excited states it is highly reactive. This reactivity accounts for the majority of photodegradation which occurs with pressure sensitive paints [63, 64]

Taking measurements with pressure sensitive paint is typically done in one of two ways. The first method is based on the relative intensity change between the "wind-off" image and the "wind-on". The wind-off image is the reference image that is taken when there is no fluid motion interacting with the test specimen. In the wind-off images, the energy dissipation routes of luminescence and oxygen quenching are still

active. This gives an image with reference or base intensity values which can then be used later. The wind-on image is taken when the desired flow phenomenon is occurring on or around the test specimen. The subsequent fluid-solid interactions either increase or decrease the local pressures and, in turn, the local partial pressures of oxygen. Due to the relative change in oxygen concentration, the intensity distribution due to luminescence differs from that of the wind-off image. The two images are then used to create and intensity ratio in which the reference, or wind-off image, is divided by the wind-on image. From here, the Stern-Volmer relationship is utilized, which is shown in Equation 1.46:

$$\frac{I_{ref}}{I} = A + B\frac{p}{p_{ref}} \tag{1.46}$$

where p_{ref} is the ambient pressure associated with the wind-off image. Equation 1.46 is then solved for p to give the static pressure at any point on the surface of the test specimen. The coefficients A and B are temperature dependent; however, for PtTFPP luminophore a good starting point is: $A = 0.2$ and $B = 0.8$. This method for taking PSP measurements is known as the intensity-based, or radiometric, method [44].

The second method is referred to as the lifetime method. This method is dependent upon the luminescent lifetime of the given paint and the associated dependency on local pressure [44]. The luminescent response of an excited particle can be modeled with the first order system given in Equation1.47:

$$\frac{dI}{dt} = -\frac{I}{\tau} + E(t) \tag{1.47}$$

where, I is the intensity, τ is the luminescent lifetime [48,52,65], and $E(t)$ is the time dependent illumination (the illumination intentionally supplied by the experimental light source). For the purposes of the lifetime method, $E(t)$ is typically short and is negligible, thus making the solution to Equation 1.47 an exponential decay:

$$I(t) = I_0 \mathrm{e}^{-t/\tau} \tag{1.48}$$

where I_0 is the initial intensity. Oxygen quenching, being the method by which both the radiometric and lifetime methods operate, allows for the relationship between luminescent lifetime and air pressure to again be represented using the Stern-Volmer relationship given in Equation 1.49:

$$\frac{\tau_{ref}}{\tau} = A + B\frac{p}{p_{ref}} \tag{1.49}$$

where the subscript *ref* indicates a value attributed to the wind-off scenario. The typical measurement process used when employing the lifetime measurement tech-

nique utilizes two gated images collected at different moments along the exponential decay of the luminophore.

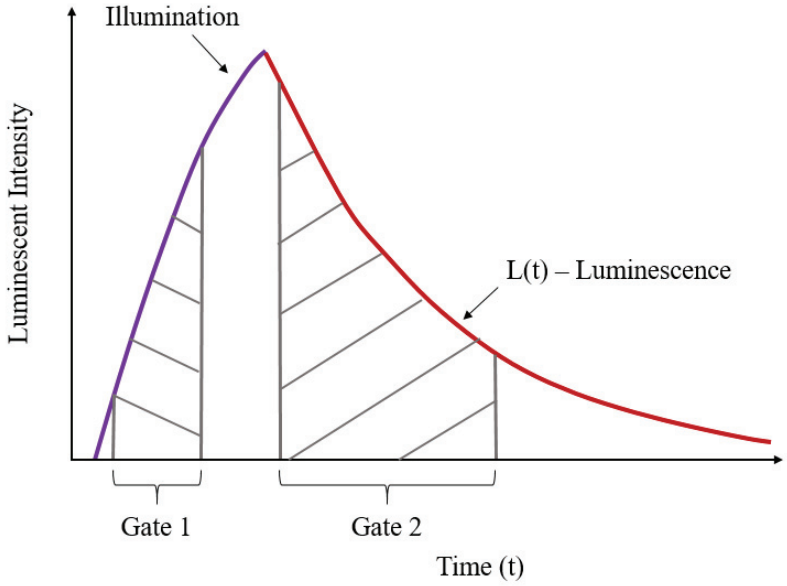

Figure 1.6: Two-gate lifetime measurement method (Adapted from [4])

The first gate is triggered during the excitation period of the curve [4]; here the pressure sensitivity of the paint is fairly low [44]. The second gate is triggered after the illumination pulse has completed and captures the exponential decay associated with the luminescent lifetime of the paint. During this period in the decaying process, the paint is much more susceptible to changes in pressure [44]. The gated images can then be integrated with respect to time to give the modified Stern-Volmer relationship shown in Equation 1.50:

$$\frac{(I_{G2}/I_{G1})_{ref}}{I_{G2}/I_{G1}} = A + B\frac{p}{p_{ref}} \tag{1.50}$$

here, the subscripts *G1* and *G2* refer to the temporally integrated intensity values associated with the first and second gates respectively. A general plot of the illumination and subsequent exponential decay of a luminophore molecule along with regions indicating the first and second gates is shown illustrated in Figure 1.6.

Given sufficient pressure drop along with intentional experimental design, either of the PSP measurement techniques discussed above (radiometric or luminescent lifetime) can be valuable tools for measuring previously challenging internal flows. The implementation of PSP in these regards, including experimental setup and processing of data, will be discussed further in Chapters 2.3 and 5.2.

1.3 Computational Fluid Dynamics

As discussed in Section 1.2, taking measurements of the flow field within a cyclone separator can be a difficult task. Typical measurement techniques disturb the flow, thus creating a need for experimental campaigns using more innovative techniques. As a result, many attempts have been made to produce accurate simulated results of the flow phenomena. Yet, successful and truly accurate numerical results, are notoriously difficult to produce. This is owed to the highly turbulent and anisotropic flow within the cyclone separator. The various methods by which many authors have ventured to acquire numerical data on the cyclone separator flow field have various advantages and disadvantages. Often, the researcher will have to accept certain inaccuracies in exchange for more reasonable computing times.

1.4 Turbulence Modeling

Before introducing the specific cases where turbulence models have been employed in attempts to model vortex flow in cyclones, a review of how turbulence models function must first be discussed. This will lend itself to a better understanding of why certain models fail to predict certain features in cyclone flow. The most modern computational fluid dynamics (CFD) software packages employ three different methods for modeling turbulent flow. The most common methods involve ensemble-averaging or time-averaging of fluctuating quantities. To do this, first instantaneous quantities are decomposed into mean and fluctuating values; where, in tensor notation:

$$u_i = \overline{u_i} + u_i' \tag{1.51}$$

here, $\overline{u_i}$ is the average component and u_i' is the fluctuating component. It is assumed that, once averaged, $\overline{u_i'} = 0$. Inserting these quantities into the instantaneous Navier-Stokes equations, and taking the time-averaged value, yields the Reynolds-averaged Navier-Stokes (RANS) equations of motion:

$$\frac{\partial \rho}{\partial t} + \frac{\partial}{\partial x_i}(\rho \overline{u_i}) = 0 \tag{1.52}$$

$$\frac{\partial}{\partial t}(\rho \overline{u_i}) + \frac{\partial}{\partial x_j}(\rho \overline{u_i}\,\overline{u_j}) = -\frac{\partial p}{\partial x_i} + \frac{\partial}{\partial x_j}\left[\mu\left(\frac{\partial \overline{u_i}}{\partial x_j} + \frac{\partial \overline{u_j}}{\partial x_i} - \frac{2}{3}\delta_{ij}\frac{\partial \overline{u_k}}{\partial x_k}\right)\right] + \frac{\partial}{\partial x_j}(-\rho\overline{u_i'u_j'}) \tag{1.53}$$

where δ_{ij} is the Kronecker delta and $-\rho\overline{u_i'u_j'}$ are Reynolds stresses. These require additional equations to account for the additional terms — the Reynolds stresses [66]. The most common RANS turbulence models, k-ϵ and k-ω, introduce two new equations, which are then used to solve for turbulent viscosity or eddy viscosity, and

in turn, Reynolds stresses. These models employ the Boussinesq hypothesis:

$$-\rho\overline{u_i'u_j'} = \mu_t\left(\frac{\partial\overline{u_i}}{\partial x_j} + \frac{\partial\overline{u_j}}{\partial x_i}\right) - \frac{2}{3}\left(\rho k + \mu_t\frac{\partial\overline{u_k}}{\partial x_k}\right)\delta_{ij} \tag{1.54}$$

where μ_t is the turbulent viscosity and and k is turbulent kinetic energy. This approximation assumes the turbulent viscosity is a scalar quantity solved for, using turbulent kinetic energy and either turbulent dissipation rate ,ϵ, or specific dissipation rate, ω. In both of these models, k and ϵ or ω are put into transport equations that account for the temporal and convective evolution of the given quantity as well as various diffusion and production terms. After solving for k and ϵ, turbulent viscosity is calculated using:

$$\mu_t = \rho C_\mu\frac{k^2}{\epsilon} \tag{1.55}$$

where, $C_\mu = 0.09$. This turbulent viscosity is then related to the Reynolds stresses using the mean velocity gradients shown in Equation 1.54. The addition of only two transport equations allows for solutions to be found for turbulent flows quickly. However, this concise closure of the RANS equations yields a diminished view of the Reynolds stresses. For this reason, the $k-\epsilon$ model has proven to be inadequate in modeling the highly anisotropic turbulent flow found within a cyclone separator [5,67].

While the $k-\epsilon$ model has been shown to predict a forced-vortex velocity field, the re-normalizable group (RNG) $k-\epsilon$ model is able to resolve a version of the combined vortex found in cyclone flow [5]. This turbulence model can then be used to "initialize" a model before employing the computationally intensive Reynolds Stress Model [68]. The Reynolds Stress Model (RSM), rather than using the Boussinesq hypothesis, resolves all six components of the Reynolds stress tensor. This is accomplished by taking moments of Equaiton 1.53 and then time averaging the respective products [69]:

$$\frac{\partial}{\partial t}(\rho\overline{u_i'u_j'}) + \frac{\partial}{\partial x_k}(\rho u_k\overline{u_i'u_j'}) = -D_{T,ij} + D_{L,ij} - P_{ij} - G_{ij} + \phi_{ij} - \epsilon_{ij} - F_{ij} + S_{user} \tag{1.56}$$

where $D_{T,ij}$ is the turbulent diffusion term which can be modeled by:

$$D_{T,ij} = \frac{\partial}{\partial x_k}\left(\frac{\mu_t}{\sigma_k}\frac{\partial\overline{u_i'u_j'}}{\partial x_k}\right) \tag{1.57}$$

here, $\sigma_k = 0.82$. In Equation 1.56, $D_{L,ij}, P_{ij}$ and F_{ij} are molecular diffusion, stress production, and system rotation, respectively; which are resolved exactly using:

$$D_{L,ij} = \frac{\partial}{\partial x_k}\left[\mu\frac{\partial}{\partial x_k}(\overline{u_i'u_j'})\right]; \tag{1.58}$$

$$P_{ij} = \rho\left(\overline{u_i'u_j'}\frac{\partial u_j}{\partial x_k} + \overline{u_j'u_k'}\frac{\partial u_i}{\partial x_k}\right); \tag{1.59}$$

$$F_{ij} = 2\rho\Omega_k\left(\overline{u_j'u_m'}\epsilon_{ikm} + \overline{u_j'u_m'}\epsilon_{jkm}\right) \tag{1.60}$$

Similarly to the turbulent diffusion term, $D_{T,ij}$, buoyancy production, pressure strain, and turbulent dissipation represented in Equation 1.56 by G_{ij}, ϕ_{ij}, and ϵ_{ij}, respectively, need to be modeled. The buoyancy production term is not relevant to this work due to negligible fluctuations in fluid temperature and density. To model the pressure strain, ϕ_{ij}, a number of different methods are available. It is most often modeled using the following decomposition as a base,

$$\phi_{ij} = \phi_{ij,1} + \phi_{ij,2} + \phi_{ij,w} \tag{1.61}$$

where $\phi_{ij,1}$ and $\phi_{ij,2}$ are the slow and rapid pressure strain terms, respectively. $\phi_{ij,w}$ is the wall reflection term, which is responsible for redistributing normal stresses near the wall [66]. Specifically, the slow and rapid pressure strains are modeled by,

$$\phi_{ij,1} \equiv -C_1\rho\frac{\epsilon}{k}\left[\overline{u_i'u_j'} - \frac{2}{3}\delta_{ij}k\right] \tag{1.62}$$

$$\phi_{ij,2} \equiv -C_2\left[\left(\frac{P_{ij} + F_{ij} + 5}{6G_{ij} - C_{ij}}\right) - \frac{2}{3}\delta_{ij}\left(\frac{P + 5}{6G - C}\right)\right] \tag{1.63}$$

where $C_1 = 1.8$, $C_2 = 0.60$, $P = \frac{1}{2}P_{kk}$, $G = \frac{1}{2}G_{kk}$, and $C = \frac{1}{2}C_{kk}$.Finally, the wall-reflection pressure strain term is defined by,

$$\begin{aligned}\phi_{ij,w} \equiv C_1'\frac{\epsilon}{k}\left(\overline{u_k'u_m'};n_kn_m\delta ij - \frac{3}{2}\overline{u_i'u_k'}n_jn_k - \frac{3}{2}\overline{u_j'u_k'}n_in_k\right)\frac{C_lk^{3/2}}{\epsilon d} \\ + C_2'\left(\phi_{km,2}n_kn_m\delta_{ij} - \frac{3}{2}\phi_{ik,2}n_jn_k - \frac{3}{2}\phi_{jk,2}n_jn_k\right)\frac{C_lk^{3/2}}{\epsilon d}\end{aligned} \tag{1.64}$$

where $C_1' = 0.50$, $C_2' = 0.3$, n_k is the unit normal to the wall in the k direction, d is the normal distance to the wall, and $C_l = C_\mu^{3/4}/\kappa$ in which $C_\mu = 0.09$ and κ is the von Kármán constant defined as $\kappa = 0.4187$. The last term in Equation 1.56 that needs to be modeled is ϵ_{ij}, the turbulent dissipation rate. The turbulent dissipation rate tensor is describe by,

$$\epsilon_{ij} = \frac{2}{3}\delta_{ij}(\rho\epsilon + Y_M) \tag{1.65}$$

where Y_M accounts for dilation dissipation in the event that the fluid is traveling at near supersonic velocities and thus undergoing compression. For the purposes of this work, the dilation dissipation term is negligible. ϵ, in Equation 1.65, is then solved for using the transport equation,

$$\frac{\partial}{\partial t}(\rho\epsilon) + \frac{\partial}{\partial x_i}(\rho\epsilon u_i) = \frac{\partial}{\partial x_j}\left[\left(\mu + \frac{\mu_t}{\sigma_\epsilon}\right)\frac{\partial \epsilon}{\partial x_j}\right] C_{\epsilon 1}\frac{1}{2}[P_{ij} + C_{\epsilon 3}G_{ij}]\frac{\epsilon}{k} - C_{\epsilon 2}\rho\frac{\epsilon^2}{k} + S_\epsilon \quad (1.66)$$

where $\sigma_\epsilon = 1.0$, $C_{\epsilon 1} = 1.44$, $C_{\epsilon 2} = 1.92$, S_ϵ is a user defined source term, and $C_{\epsilon 3}$ is calculated by,

$$C_{\epsilon 3} = \tanh\left|\frac{v}{u}\right| \quad (1.67)$$

here, v is the velocity component parallel to the gravitational vector and u is the component of velocity perpendicular to the gravity vector. The Reynolds Stress Model discussed above has been used extensively in the study of cyclone separators [5,14,68, 70,71]. The ability to capture anisotropic turbulence in the flow gives the Reynolds Stress Model an advantage over the simpler, yet less computationally expensive, two-equation models — such as $k-\epsilon$ or $k-\omega$. While the computational resources required to run a Reynolds Stress Model are demanding, a RSM is computationally cheaper than scale-resolving methods such as LES.

Large Eddy Simulations (LES) allow for a range of turbulent length scales to be directly solved rather than modeled. To accomplish this, a filter function must be used to determine which length scales are directly resolved and which are modeled. For many CFD software packages this filter function is automatically generated as a function of the mesh created [66]. As a result, the corresponding mesh must be sufficiently dense to produce control volumes of the same characteristic length as the smallest turbulent eddies that are to be resolved. This can dramatically increase the computing power and time required. Although LES simulations are computationally expensive, some features, such as the PVC, are able to be captured in these simulations [5,38,70,72].

The most computationally expensive method, is that of direct numerical simulation (DNS). This method does not require any form of modeling to resolve the flow. As the name suggests, the smallest length and time scales of turbulence are resolved, which requires immensely dense meshes and short time-steps. Due to these high costs, at this point in the evolution of computer power and efficiency, DNS has not become a routine design tool in industry.

1.5 Problem Statement

The further the knowledge base in the field of separation technology, specifically as it applies to cyclone separators, a set of novel pressure measurements taken using PSP along the interior cone wall of a cyclone separator are desired. While there exists no shortage of computational literature on the subject — which would be expected to yield sufficient understanding of the flow field at hand — the highly anisotropic turbulence in a cyclone separator makes it difficult to yield an accurate converged solution. Furthermore, experimental analysis of the flow field has been limited to point measurements lending only limited details of the turbulent structure inside. The optical measurement campaign and corresponding computational simulations are intended to produce a higher fidelity description of the flow in the cyclone separator. Additionally, successful collection of PSP data from this specific internal flow will aim to extend the proven capabilities of the optical measurement technique to this internal flow.

Chapter 2. Experimental Setup

The experimental campaign outlined in this work was completed with the intent to introduce pressure-sensitive paint measurements to knowledge base of cyclone separators. Certain variations from the typical cyclone design were required to allow for the implementation of PSP measurements. While the basic operating characteristics of the cyclone remained the same, the materials, fabrication techniques, and assembly of the cyclone were chosen and implemented with an inclination towards experimental feasibility.

2.1 Cyclone Fabrication

Many commercial cyclone separators are produced using sheet metal which is then riveted together. This typical process, however, would not be conducive to an optical measurement campaign. Rather, the cyclone used was produced in three different parts each consisting of a different material and serving a different purpose. The barrel, or cylinder, of the cyclone was additively manufactured using a typical fused deposition modeling (FDM) printing style. In reference to Figure 3.2, the cylinder body and inlet were both created as one part using the FDM method. The cone of the cyclone separator was produced in two different pieces separated in half, down the center of the cone. This was done to allow for easy access to one half of the cone for application of the pressure-sensitive paint. The half of the cone on which PSP was applied was another additively manufactured part; this piece, however, was created using a stereolithography (SLA) printing method. The other half of the cone was fabricated using cast acrylic. The material selection for this piece was of paramount importance. Many commonly used "transparent" plastics such as polycarbonate filter light in the UV spectrum. For PSP applications, cast acrylic or quartz glass — which allow over 92 % UV transmission — should be used.

To form the cast acrylic sheet into a cone, the sheet was heated in a ceramic furnace for ten minutes at approximately 143 °C. To ensure a uniform temperature distribution in the acrylic sheet, the acrylic was placed in the furnace while it was heating to 143 °C. After the furnace reached the set temperature, the sheet spent an

additional ten minutes in the furnace. Once removed, the extremely pliable acrylic was draped over the 3-D printed half of the cone, which acted as a form. Before draping, a thin piece of wool was placed on the form to prevent the soft acrylic sheet from adhering to the part. Once the acrylic sheet was draped over the form, and bottom layer of wool, an additional piece of wool was placed on the acrylic. This allowed for smoothing and forming of the pliable acrylic without indenting or marking the surface. Besides protecting the transparent acrylic from marks and scratches on both sides, the wool acted as an insulator giving adequate time for shaping the part before it cooled.

To attach both halves of the cone and the cylinder, flanges with a bolt pattern were incorporated into the designs. For the additively manufactured parts, the flanges and bolt pattern were simply printed with the rest of the part. The acrylic half of the cone required additional fabrication. Both the semicircular flange and the two straight flanges for the acrylic cone half were manufactured by laser cutting a cast acrylic sheet. This allowed for maximum control over geometry and bolt pattern placement. The flanges were then attached to the main body by use of an acrylic adhesive. The three parts of the cyclone were then assembled with insulation foam-tape placed between all mating faces. The insulation tape minimized leakage from the cyclone during operation. To complete the cyclone assembly, two additional parts were manufactured by means of FDM printing. First, an adapter was made which allowed the cyclone to attach to an existing benchtop blower unit. Second, an end-cap was produced that could be quickly connected to the particle outlet end of the cone to convert the cyclone from and open to closed configuration.

The sizing of each part of the cyclone separator was driven by experimental needs when possible. In order to best capture the pressure drop along the cone of the cyclone, a large pressure drop was desired. To achieve this a few geometric parameters were optimized. The difference between the vortex finder radius, R_x, and the cyclone barrel radius, R was configured such that it was the same dimension as the inlet width. This setup maximized the acceleration of the entering fluid due to the "squeezing" effect from the already circulated fluid in the system. Since the inlet width was forced based on the benchtop blower dimensions, and the vortex finder diameter was determined based on readily available PVC pipe dimensions, the radius of the barrel was adjusted to maximize inlet acceleration. Additionally the diameter of the particle outlet was made sufficiently small to increase the maximum tangential velocity in the system. Both of these design parameters, which led to greater tangential velocities, produced a greater pressure drop across the cyclone separator [2, 14, 40, 73].

2.2 Benchtop Blower and Cyclone Setup

The experimental cyclone was setup as a blower configuration (i.e. fluid was pushed through the device through the tangential inlet rather than being pulled through the vortex finder). This was done using a TecQuipment benchtop blower unit which was powered via a 480 V three-phase outlet. The flow rate supplied by the benchtop blower was controlled using a potentiometer. For the purposes of this work, all experimetal data was collected with the benchtop blower operating at full power. The "full power" setting on the blower produced various inlet velocites depending on the configuration of the cyclone. The no load velocity at the contraction exit was 30 m/s. For the open configuration, full power corresponded to an inlet velocity of 18 m/s, while for the closed configuration, the inlet velocity was lowered to only 12 m/s. This decrease in inlet velocity was caused by the change in load that the blower experienced during operation. The TecQuipment benchtop blower came equipped with clasp attachments which were utilized to connect the cyclone to the blower using the inlet adapter discussed in Section 2.1. Figure 2.1 shows the barrel section of the cyclone attached to the blower.

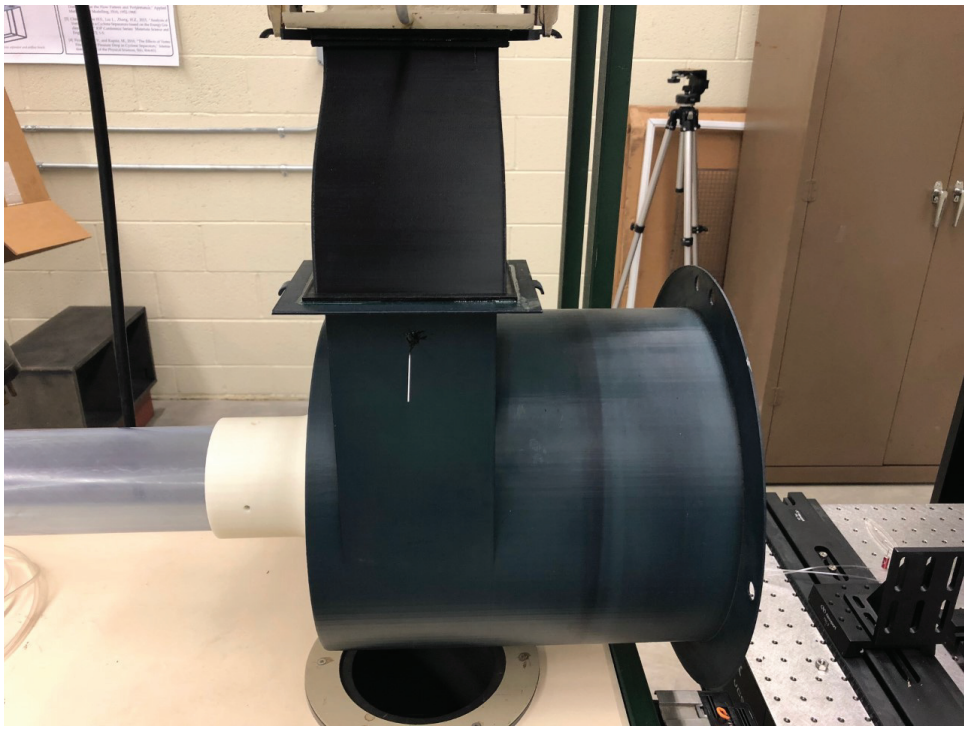

Figure 2.1: Benchtop blower with cyclone barrel.

The two cone halves were attached together using a six-hole bolt pattern in which one of the holes was used to attached the assembled cone to a vibration damping optical workbench. This connection to the optical bench not only minimized part

Figure 2.2: Additively manufactured and cast acrylic cone halves

movement during cyclone operation, but also allowed for repeatable and accurate placement of the experimental setup. Figure 2.2 shows the two cone halves assembled before being connected to the barrel and optical workbench. Each straight flange on the cone had three half-inch clearance holes. The middle clearance hole in Figure 2.2 was used two ground the cone to the optical workbench.

Figure 2.3 displays the cone assembly connected to the optical workbench. The blue tape at the base of the cone was used to prevent the reflection of both excitation and luminescent light when collecting data. The full cyclone assembly is shown in Figure 2.4. Finally, the endcap, which allowed for the cyclone to be converted from and open to closed configuration, was placed using a slide system connected to the optical workbench. Insulation foam was placed on the endcap to prevent leakage during operation.

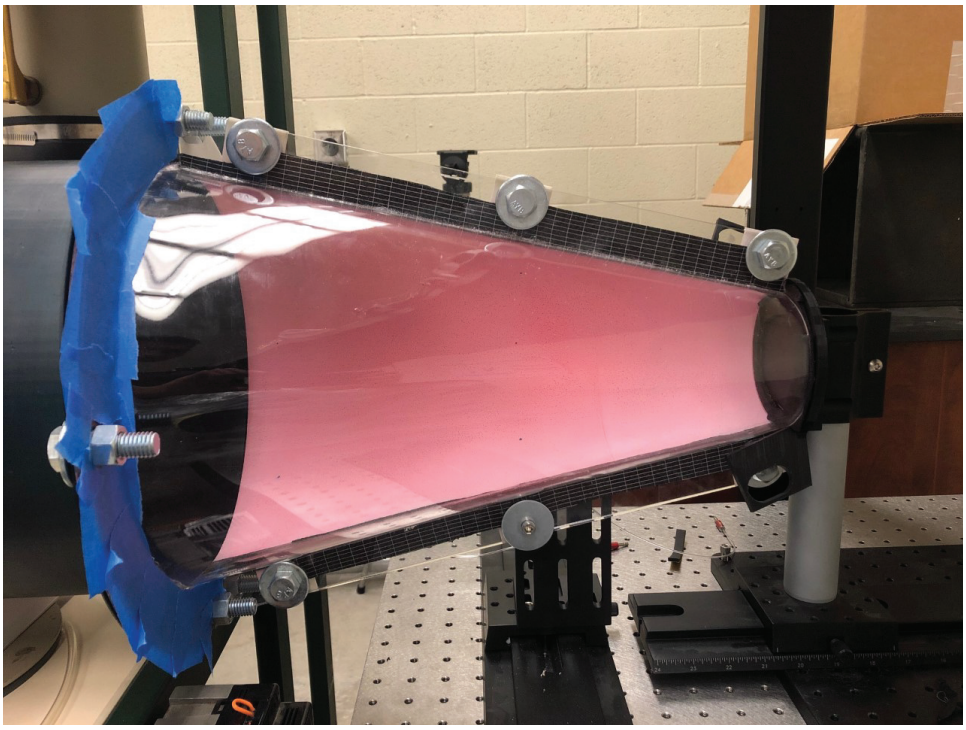

Figure 2.3: Cone assembly mounted to optical workbench.

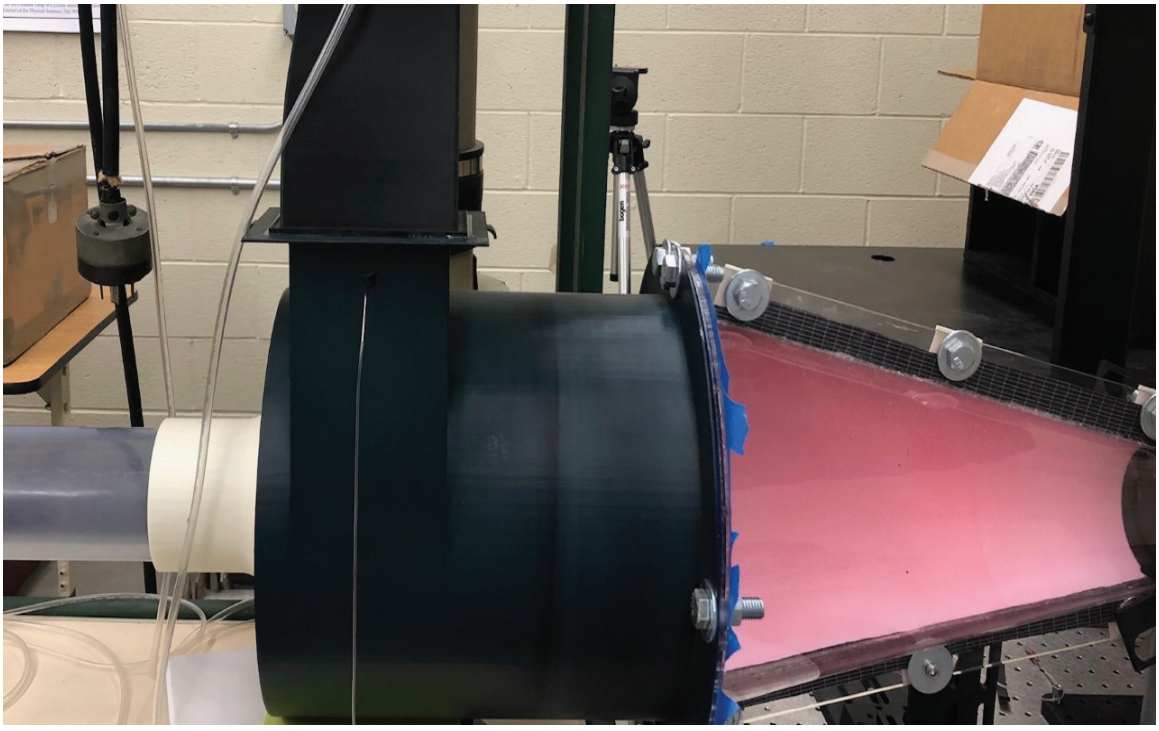

Figure 2.4: Experimental cyclone setup.

To quantify the inlet velocity of the cyclone, a pressure tap available just after

the blower contraction was used. The static pressure measured at this point was used with the static pressure taken in the settling chamber of the benchtop blower. The static pressure difference between these two points was then used to calculate the inlet velocity using Equation 2.1:

$$v_{in} = \sqrt{\frac{2\Delta p}{\rho}} \tag{2.1}$$

Using Equation 2.1, two inlet velocities were calculated (12 m/s and 18 m/s) dependent on the outlet configuration. After determining the inlet velocity, v_{in}, the average volumetric flow rate was estimated at the inlet. To do this, the inlet velocity calculated in Equation 2.1 was assumed to be the average inlet velocity for the rectangular inlet ($A_{in} = 0.005\ m^2$). With this assumption, Equation 2.2 was used to estimate the volumetric flow rate for each configuration ($Q = 0.06\ m^3/s$ and $Q = 0.09\ m^3/s$):

$$Q = v_{in} A_{in} \tag{2.2}$$

2.3 Camera and Lighting Setup

Two excite the pressure-sensitive paint and capture the corresponding luminescent light, a combination of two high-power UV LEDs (Innovative Scientific Solutions, Inc. LM2xLZ-400 Lamp Module) and one 14-bit CCD camera (pco.1600) were used. The two high-power LEDs pulsed 400 nm UV light signaled by a signal generator (Innovative Scientific Solutions, Inc. PSG-3 Pulse Delay Generator) at four Hertz with a nine millisecond pulse. The CCD camera was triggered by the same signal generator with a one millisecond offset from rising edge of the LED signal allowing for eight milliseconds of exposure time per image. The high-power LED is shown in Figure 2.5.

The camera exposure time and binning was controlled via pco.camware software. A 28 mm lens with a longpass and antiglare filter were used in conjuction with the CCD camera. The zoom, focus, and aperture settings for the lens were controlled with an Innovative Scientific Solutions, Inc. LC-2 Lens Controller. Settings for zoom, focus, and aperture size were set at the start of each data collection trial to account for varying luminophore excitation. Attached to the longpass filter was an antiglare filter that reduced the amount of diffuse scattered excitation light. A total of 256 images were captured for ensemble averaging. Given the settings discussed above, it took 64 seconds to capture all images. The number of images taken was determined by finding a balance between increasing signal-to-noise ratio with high image count, and minimizing the total paint illumination time to prevent photo-degradation. The

Figure 2.5: ISSI high-power UV LED lamp module.

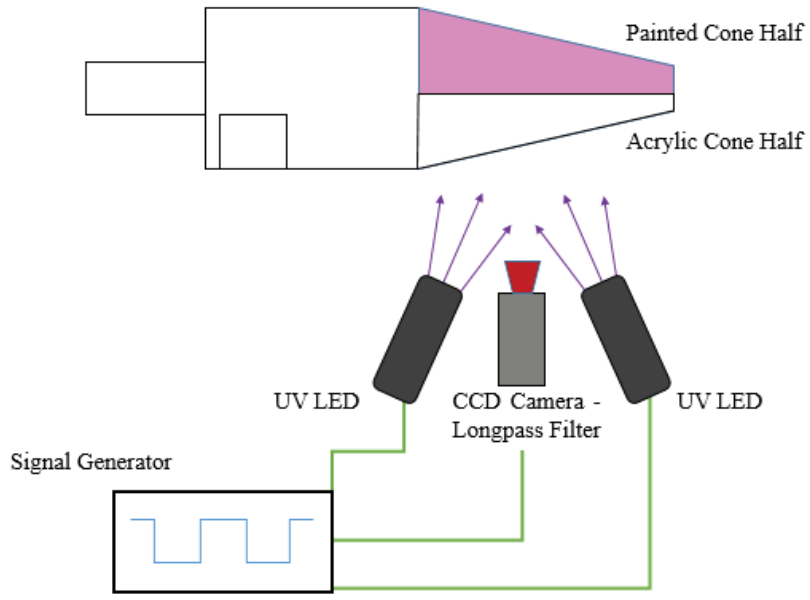

Figure 2.6: Schematic of PSP setup.

final number of images, 256, proved to allow for sufficient signal strength for post processing while not incurring much error due to over-illumination of the paint. A schematic of the entire PSP setup is illustrated in Figure 2.6. The schematic displays the setup from a top view. Both LEDs along with the CCD camera were mounted to a passively damped Newport optical table.

Chapter 3. Numerical Setup

For implementation in CFD, the cone, cylinder, and inlet were modeled together as a single volume shown in Figure 3.2. The CFD calculations presented must satisfy a number of criteria before the results received from the model can be accepted as accurate. One of the most crucial components for any CFD model is the choice of a turbulence model. ANSYS Fluent offers a multitude of different turbulence models that each have a range of applications for which they are accurate. As mentioned in Section 1.4, a k-ϵ model with the proper settings for swirling flow can be implemented as a means to achieve initial convergence [68]. However, a k-ϵ model calculates flow fields by assuming that the turbulent stresses are isotropic. Physically, the cyclone vortex is expected to exhibit a high degree of anisotropy. For these reasons, a linear pressure-strain Reynolds Stress Model (RSM) was chosen to account for the effects of anisotropy, which solves the second-order moment equations for all six components of the Reynolds stress tensor along with a diffusion component [66, 69, 74].

Table 3.1: Cyclone dimensions corresponding to figure 3.1

D	11.0 in (0.28 m)
H/D	2.545
L/D	1.091
V/D	0.909
D_e/D	0.318
D_i/D	0.279
A/D	0.179
B/D	0.357
C/D	0.096

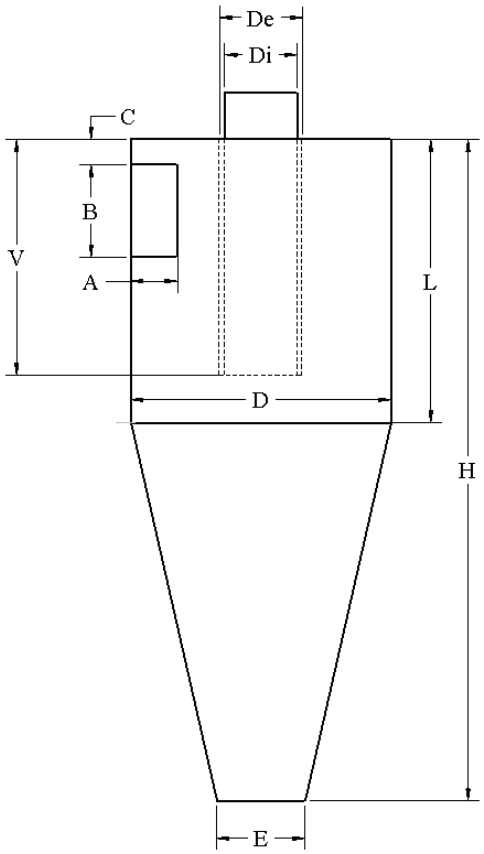

Figure 3.1: Parameters for cyclone geometry definition

The CFD calculations were performed using ANSYS Fluent 19.1. The default coefficients suggested by the program for the RSM — which are also reviewed in Section 1.4 — were utilized. No other suggestions were found for these terms in the literature. A transient analysis was used in order to capture the cyclic nature of the flow [70]. Two different models of interest were run for data collection. The first having an "open" setup, meaning that the end of the cone through which particulate matter exits (the narrow end of the cone) was left open. As second configuration, which will be referred to as the "closed" configuration placed a wall boundary condition at the narrow end of the cone. The boundary conditions for each configuration were driven by the experimental campaign. As such, the inlet velocity placed at the inlet of both CFD configurations differed between the two simulations to match the output of the experimental setup. For the open configuration, an inlet velocity of 18 m/s was imposed at the inlet, while for the closed configuration a 12 m/s inlet was used. As previously mentioned, the open configuration imposed a 0 Pa (gauge) boundary condition at the opening at the narrow end of the cone, which differed from the stationary wall boundary placed in the same location in the closed configuration.

Both models used a 0 Pa (gauge) outlet at the end of the vortex finder to simulate that exit being open to ambient conditions. All other surfaced in both configurations were modeled as stationary walls with a no slip boundary condition. A summary of the boundary conditions used for each configuration are found in Table 3.2.

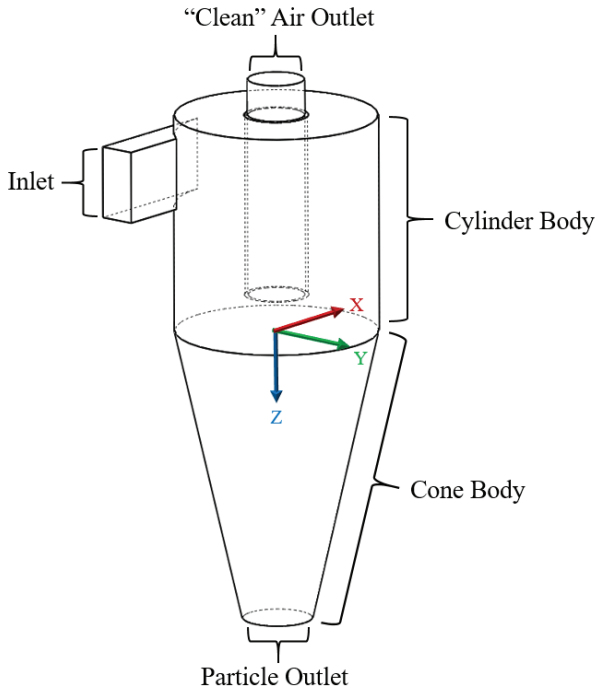

Figure 3.2: Nomenclature and Cartesian axes for key features of cyclone

Table 3.2: CFD boundary conditions for open and closed configurations.

Boundary	Open Configuration	Closed Configuration
Inlet	18 m/s Velocity Inlet	12 m/s Velocity Inlet
Particle Outlet	0 Pa (gauge) Pressure Outlet	Stationary Wall (no-slip)
Vortex Finder Outlet	0 Pa (gauge) Pressure Outlet	0 Pa (gauge) Pressure Outlet
Walls	Stationary Wall (no-slip)	Stationary Wall (no-slip)

$$t_{res} = \frac{V}{Q} \tag{3.1}$$

The time step for a transient analysis should be a small fraction of the flow residence time [75]. Using Equation 3.1, a residence time of 0.348 seconds was calculated for the open configuration simulation, while a residence time of 0.522 seconds was calculated for the closed configuration. For both simulations a time-step of 1 millisecond was used, as it was several orders of magnitude smaller than both residence times.

3.1 Mesh Generation and Convergence

The final mesh used for both the open and closed simulations was first proven to produce results which were independent of the mesh sizing and spacing. To do this, three different meshes were run on the open configuration, at a higher inlet velocity and corresponding Reynolds number. From these three simulations, pressure data along the cone wall was compared as the metric of mesh convergence. In the literature, it is common to use the pressure drop across the device, from the inlet to the outlet, as a mesh convergence criteria. However, since the thrust of this work was to capture the pressure distribution along the cone wall via experimental methods, pressure data in the corresponding region was used to test mesh convergence. The three different meshes consisted of 2.8 million elements, 4.7 million elements, and 7 million elements. The computing time and processor information for each simulation is shown in Table 3.3. Time-averaged static pressure data along the cone wall was exported from Fluent for each of these simulations and processed in MATLAB. To account for the different number of control volumes in each mesh — and the corresponding number of data points exported — a 700 by 1050 equally spaced grid was created in MATLAB on which the data from Fluent was interpolated. From this grid, the data for each mesh was then compared point-wise for discrepancies. In this work, the criteria for mesh convergence was a maximum of two percent difference between any given pair of points. Table 3.4 displays results from this mesh independence study.

Table 3.3: Processor and computational time specifications.

Mesh Elements	Processor Specifications	Number of Processors	Processor Hours
2.8 Million	Intel® Core™ i7-8700	6	960
4.7 Million	Intel® Xeon™ E5-2687W v4	12	2,208
7.0 Million	Intel® Xeon™ E5-2687W v4	12	3,864

Table 3.4: Maximum percent difference in wall static pressure.

Elements in Millions	Percent Difference
2.8 vs. 4.7	11 %
4.7 vs. 7.0	1.8 %

The maximum percent difference for both trials was located at approximately 0.014 m from the particle outlet along the cone wall. Both maxima were located near the center-line of the cone wall. The results from the mesh convergence study in Table

3.4 indicate that the mesh consisting of approximately 4.7 million control volumes was sufficiently dense for producing results which were no longer dependent on the mesh sizing. For this reason the grid with 4,726,465 elements was used for both the open and closed configuration simulations. A first cell height near the walls of 0.254 mm was used in this mesh, which yielded a y^+ value less than 30 for both simulations. This y^+ value was sufficient for the simulations in this work since standard wall functions were used in near wall regions [66]. A rendering of a less dense mesh used for early computational models is shown in Figure 3.3. The cut section shown in Figure 3.3b is a section view of the same earlier mesh. The final mesh consisting of over 4.7 million control volumes was too dense to show any detail in a section view.

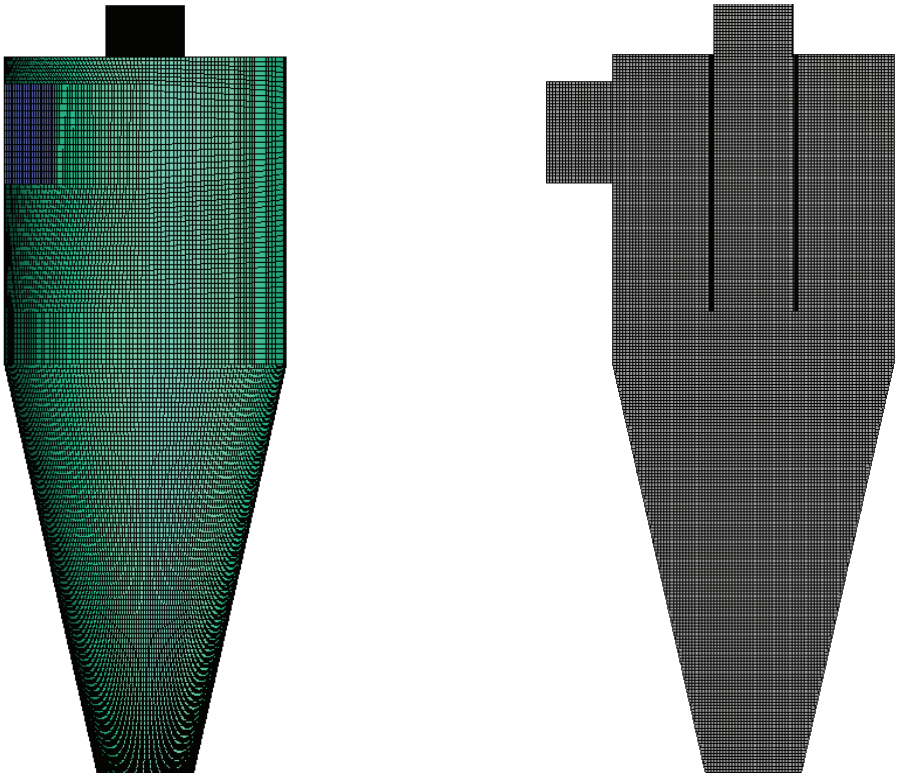

(a) (b)

Figure 3.3: (a) Full cyclone mesh.; (b) Cross-sectional view along central plane.

3.2 Spatial and Temporal Discretization Methods

For the open configuration simulation Second-order upwind equations were chosen for the spatial discretization of momentum, turbulent kinetic energy, turbulent dissipation, and Reynolds stresses. A second-order central differencing discretization was used for the pressure interpolation. A Coupled Algorithm was selected for pressure-

velocity coupling. In this formulation, the pressure and velocity terms from the momentum equation are solved for simultaneously in one matrix [66]. The second-order upwind discretization referenced above calculates the face value of any discretized term using the cell-centered value and the gradient of the term described by,

$$\phi_{f,SOU} = \phi + \nabla\phi \cdot \vec{r} \tag{3.2}$$

where ϕ is an arbitrary discretized cell-centered value, and the subscript f, SOU indicates the second-order upwind face value. ∇ represents the gradient of the discretized value in the upwind cell, and the vector $\vec{r}$ is the displacement vector going from the center of the upwind cell to the center of face f. The second-order central differencing method used for pressure interpolation is represented by the general central differencing formulation given in Equation 3.3,

$$\phi_{f,CD} = \frac{1}{2}(\phi_0 + \phi_1) + \frac{1}{2}(\nabla\phi_0 \cdot \vec{r_0} + \nabla\phi_1 \cdot \vec{r_1}) \tag{3.3}$$

where the subscript f, CD indicates the central differencing face value of the discretized term, and the subscripts 1 and 2 indicate the two cells on either side of the face represented by f. To determine the gradient of any discretized term the Lease Squares Cell Based method was implemented. This method solves the least-squares minimization problem to determine the linear variation between a cell, c_0, and a neighboring cell, c_1. This is done for any number of directions equal to the number of neighboring cells to cell c_0.

For the closed configuration cyclone the same discretization methods were implemented for turbulent kinetic energy, turbulent dissipation, and pressure interpolation. To promote spatial accuracy in the closed configuration solution, third-order monotone upstream-centered schemes for conservation laws (MUSCL) were used for momentum and Reynolds stress terms. This third-order discretization is a weighted combination of the central differencing and second-order upwind schemes previously discussed described by,

$$\phi_f = \Theta\phi_{f,CD} + (1 - \Theta)\phi_{f,SOU} \tag{3.4}$$

where, Θ is between zero and one. The value of Θ is calculated during computations in such a way as to not introduce new extrema for any given variable, ϕ [66]. The third-order MUSCL scheme can increase solution accuracy by minimizing the amount of numerical diffusion during calculations [66]. For this reason, it was implemented in the closed configuration simulation, which was expected to exhibit the highly turbulent and anisotropic flow typically observed in cyclone separators.

The transient formulation was achieved using both bounded and unbounded second-

order implicit integration. The bounded second-order integration functions much like a central differencing discretization scheme, only over a temporal element rather than a spatial one,

$$\frac{\partial \phi}{\partial t} = \frac{\phi_{n+1/2} - \phi_{n-1/2}}{dt} \tag{3.5}$$

where,

$$\begin{aligned} \phi_{n+1/2} &= \phi_n + \frac{1}{2}\beta_{n+1/2}(\phi_n - \phi_{n-1}) \\ \phi_{n-1/2} &= \phi_{n-1} + \frac{1}{2}\beta_{n-1/2}(\phi_{n-1} - \phi_{n-2}) \end{aligned} \tag{3.6}$$

in which, the subscripts $n, n+1, n-1$, and $n-2$ indicate relative time levels, and β is a bounding factor. The bounded second-order integration is only applicable to the turbulent kinetic energy and turbulent dissipation rate terms. For all other terms — momentum, Reynolds stresses, and pressure — a standard second-order integration is used,

$$F(\phi) = \frac{3\phi^{n+1} - 4\phi^n + \phi^{n-1}}{2\Delta t} \tag{3.7}$$

where $F(\phi)$ represents the integral of any quantity. ϕ^{n+1} is then solved for implicitly using $F(\phi^{n+1})$ from the neighboring cells.

Chapter 4. Experimental Error Analysis

An analysis of the error introduced to experimental measurements was completed to characterize the validity and accuracy of the results. Three possible significant sources of error in the optical measurements were photo-degradation, thermal deactivation, and camera viewing angle. These three sources were minimized by various methods which will be covered in the following sections. A certain amount of uncertainty in the computational results is also introduced due the surface roughness of the painted half of the cone. A topological study was performed to quantify these effects. Other, more typical, sources for error were quantified using statistical analysis.

4.1 Luminescent Photo-degradation

With long periods of LED exposure time, excited oxygen molecules can quickly react with PSP luminophore molecules thus reducing the fluorescent intensity of both wind-on and wind-off images. After post-processing, the artificial drop in intensity would manifest as lower pressure than was actually present. To quantify the photo-degradation of the image sets a temporal analysis of pixel intensity was completed. The images analyzed were the same as those used for calculations. This allowed for a temporal analysis over 64 seconds from the first image to the last. Figure 4.1 is a plot of the percent change between the first and last image at each pixel along the centerline of the cone (i.e. $r/R = 0$). Moreover, the horizontal axis corresponds to pixels in the captured images (taken from a 600 by 800 pixel image), while the vertical axis gives the percent difference between the first and last image of the sequence. A large range of percent differences is present along the cone; however, a linear fit of the data shows that the average percent difference is approximately 0.14%. This was accomplished by pulsing the LEDs as highlighted in Section 2.3. By pulsing the excitation LEDs, the total PSP exposure time was decreased from 64 seconds, with continuous illumination, to less than two and a half seconds with pulsed illumination.

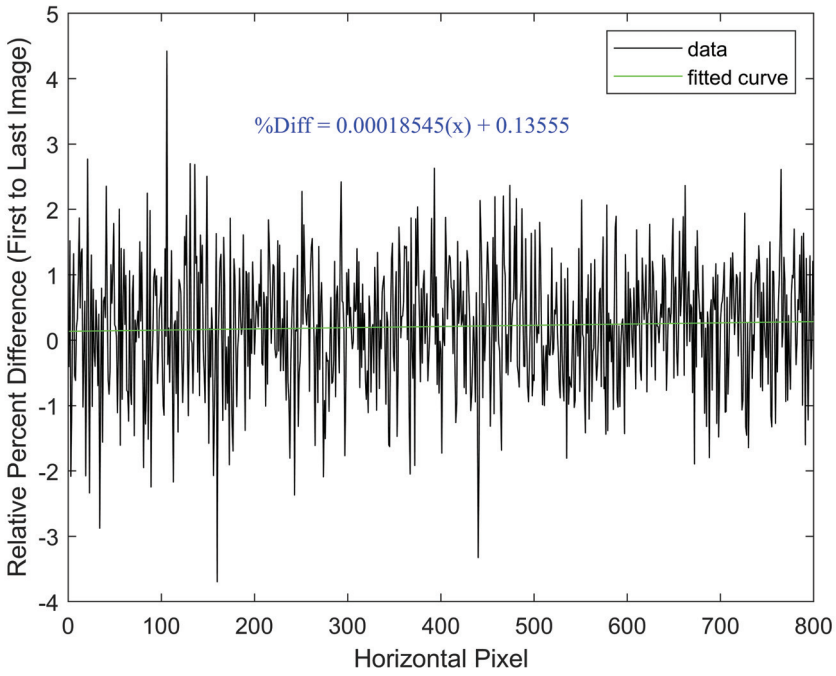

Figure 4.1: Shot-to-shot pixel intensity variation along centerline.

4.2 Thermal Deactivation

As mentioned in Section 1.2, thermal deactivation is the most common source of error when taking PSP measurements. The consequences of not quantifying and correcting the effects of thermal deactivation are incredibly high. Much like photo-degradation, thermal deactivation lowers the luminescent intensity of the paint, which then would lead to artificially low pressures after post processing. To quantify the effect of the temperature gradient across the cone, a viscous heating study was performed on the cast acrylic half of the cone. In this study, a K-type thermocouple was placed on the interior surface of the cone — the surface opposite which the PSP would be applied — and the blower unit, with the cyclone attached, was run on full power. The thermocouples were placed on the acrylic half of the cone as to preserve the already painted surface on the additively manufactured half. Since the temperature gradient between the two pressure tap points was of interest, the thermocouples were placed at axial locations equivalent to those of the pressure taps. With this placement, and the assumption that the flow was axisymmetric once time-averaged, the temperature gradient captured was equivalent to that found on the opposite half of the cone. The setup for this study is shown in Figure 4.2, with detailed images of the relative thermocouple and pressure tap placement shown in Figure 4.3.

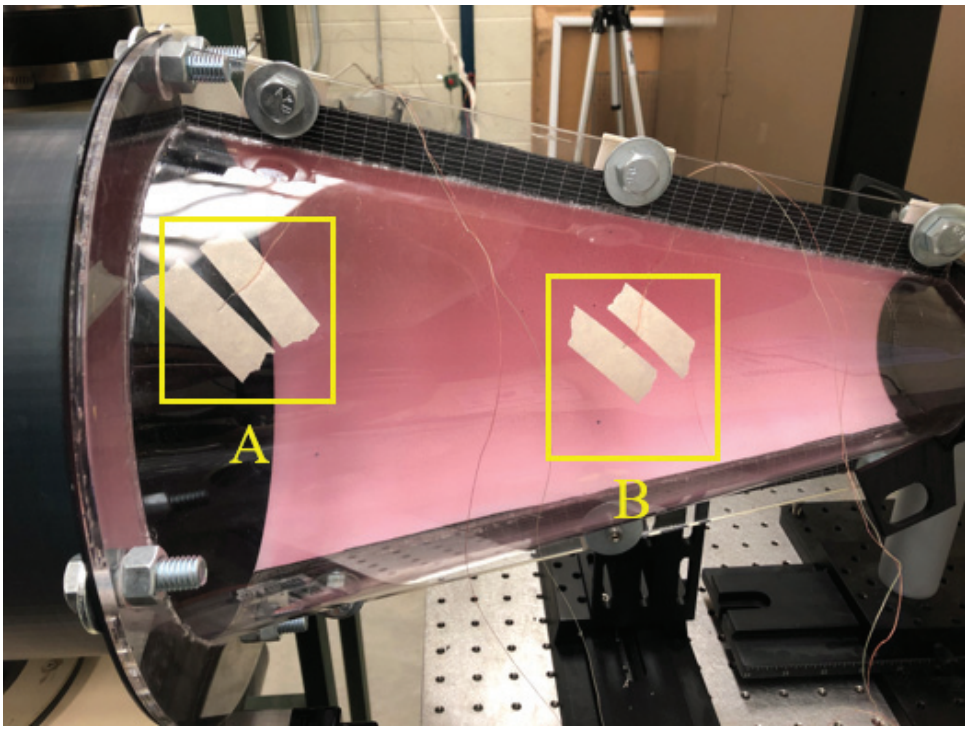

Figure 4.2: Thermocouple placement for viscous heating study.

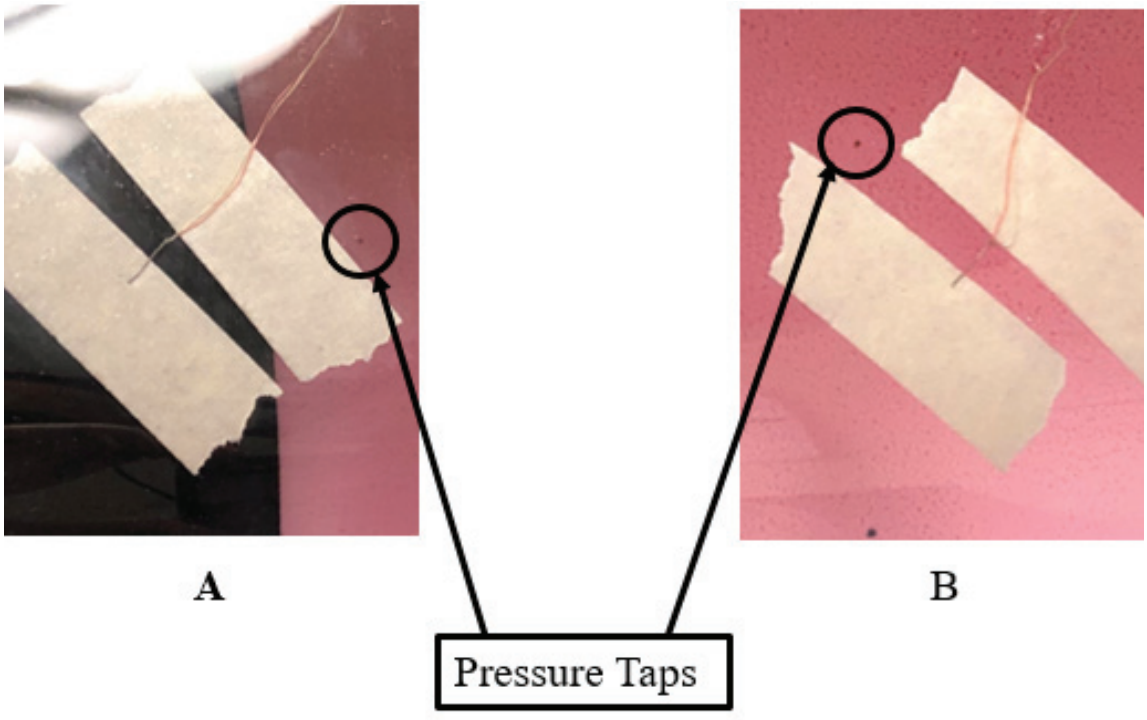

Figure 4.3: Detail views of the thermocouple placement.

The temperature of the surface of the cone was tracked over time to quantify the viscous heating. Figure 4.4 shows the temperature evolution over approximately 1200 seconds. During this time, the temperature of the cone increased by approximately three $°C$. While the temporal temperature evolution was significant, the temperature gradient between the two points at any moment in time has a greater impact on the functionality of the PSP. In Figure 4.4, a sharp increase in temperature is shown at approximately 200 seconds, which corresponds with the start of cyclone operation. The data collected before this point was used to correct for the bias error in readings between the two thermocouples. The average difference between the thermocouples was calculated to be $0.0245°C$. This value was then subtracted from the maximum temperature gradient measured during cyclone operation. After correcting for the bias error in the readings, a maximum temperature gradient of $0.1320°C$ was measured at the 745 seconds into the study.

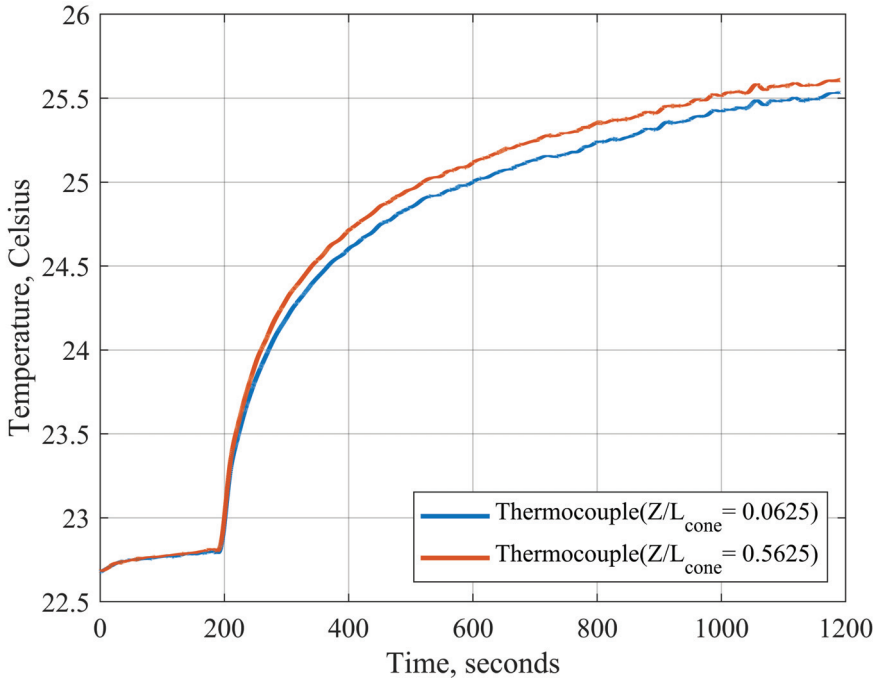

Figure 4.4: Temperature increase of cone due to viscous heating.

The thermocouple data was collected using a 24-bit National Instruments CompactRio (cRIO) NI 9211 thermocouple input module. With a voltage range of $\pm 80\ mV$, a temperature resolution of $\pm 2.35(10^{-4})\ °C$ was calculated. Factoring the resolution into the maximum temperature gradient gives $0.1320 \pm 3.33(10^{-4})\ °C$. Error bars indicating this resolution are not included in Figure 4.4 since the nominal curve and uncertainty curves would not be independently distinguishable due to the large difference in magnitude.

While the temperature gradient produced due to viscous heating was only a fraction of a degree, the impact on luminescent intensity was significant. With platinum porphyrin luminophore, a percent intensity change of approximately 0.3% is expected per degree Celsius, which leads to a drop in intensity of $0.04 \pm 1.83(10^{-4})\%$ from the measured temperature gradient. The pressure drop between the two pressure taps — which is covered later in Chapter 5 — produced a 0.08% decrease in intensity. Since the percent intensity change could be affected by up to 50% by viscous heating an *in-situ* calibration was used rather than the standard coefficients discussed in Section 1.2. The use of *in-situ* calibration accounted for the temperature dependence of the coefficients in Equation 1.46, thus minimizing error caused by viscous heating.

4.3 Camera Viewing Angle

The relative angle of the camera to the surface normal is an additional source of error for PSP measurements. Since the measurements in this work were of the curved surface of the cone interior, the viewing angle of the camera can greatly vary depending on the area imaged. The error introduced due to viewing angle has been quantified by Bencic [76]. They showed that the error was minimized to less than two percent if the camera angle did not deviate more than 75° from the surface normal. The Bencic benchmark was performed on a cylinder which has clear similarities to the cone imaged in this work. Consequently, the area imaged in this work was reduced to portions of the cone with an angle relative to the camera less than ±75°.

4.4 Surface Roughness

Pressure-sensitive paints have previously been used in a variety of external flow applications; however the substrate on which the paint is applied is most often anodized aluminum. The application of PSPs to additively manufactured materials in this work is undocumented. The successful application and measurement of the PSP in this work confirms that adhesion to the printed surface is not a problem. The question of surface roughness introduced by the painting process, however, required further investigation.

To quantify the surface roughness of the additively manufactured parts optical interferometry was utilized. First, an unpainted section of the cone was characterized using a NANOVEA optical interferometer. This device measured the surface roughness by measuring the intensity of white light reflected off the sample surface. A one square millimeter section was scanned totaling 39,082 data points and yielding an average surface roughness of 120 ± 0.258 microns with a standard deviation for the

unpainted sample of 18.4 microns. The average roughness value was then used with Equation 4.1 to determine the y^+ value. In general, a y^+ value less than five indicates that a surface can be considered hydraulically smooth.

$$y^+ = \frac{hu^*}{\nu} \tag{4.1}$$

Here, h is the surface roughness, ν is the kinematic viscosity of the fluid, and u^* is the friction velocity given by,

$$u^* = \sqrt{\frac{\tau_w}{\rho}} \tag{4.2}$$

where, τ_w is the shear stress at the wall and ρ is the fluid density. From Equation 4.1, a y^+ value of 11.6 was calculated for the unpainted section of the cone. A painted sample of the cone was then analyzed using the same NANOVEA optical interferometer. An area of one square millimeter was again analyzed with this instrument. A recreated topology of the painted and unpainted surfaces are shown in Figure 4.5 and Figure 4.6.

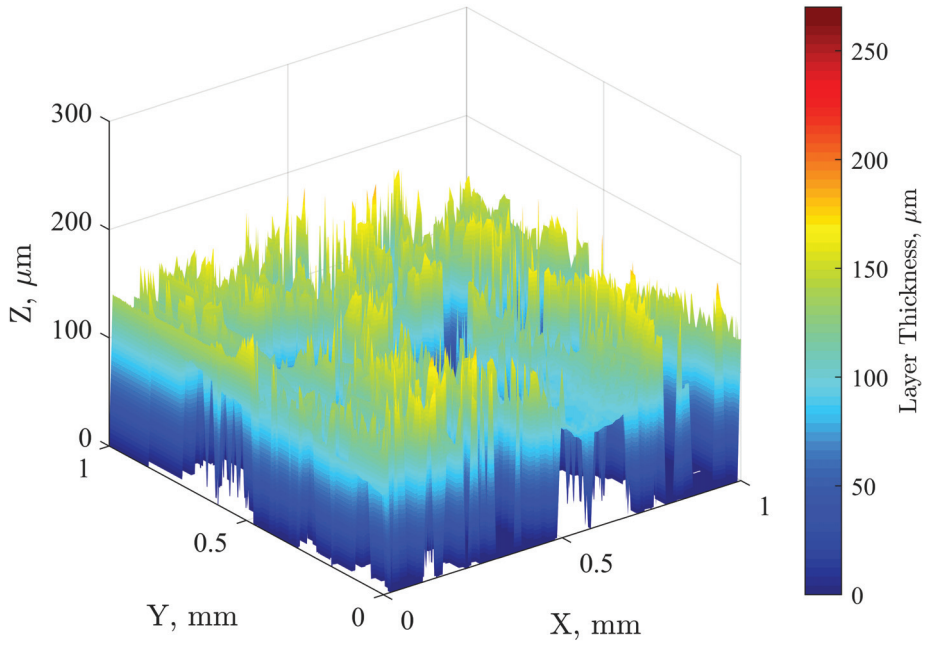

Figure 4.5: Topology of unpainted section of cone for roughness analysis.

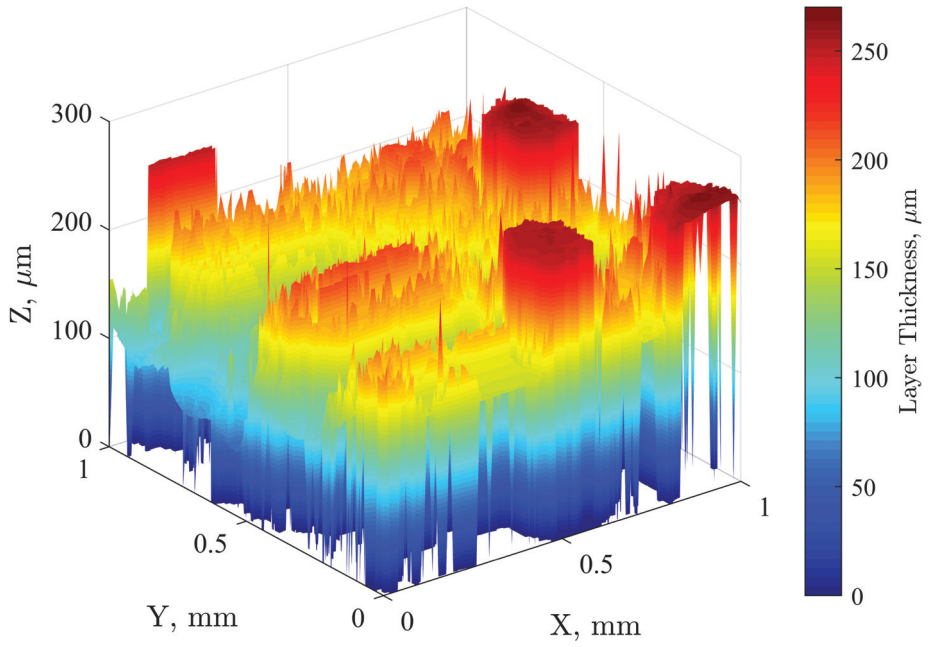

Figure 4.6: Topology of painted section of cone for roughness analysis.

The average paint layer height of the painted cone was calculated to be 165 ± 0.434 microns from the 39,082 samples collected with a standard deviation of 42.9 microns. Using the average value with Equation 4.1 yields a y^+ value of 15.9. Both of these y^+ values indicate that the additively manufactured substrate and the pressure-sensitive paint cannot be considered hydraulically smooth. Thus, from this analysis it can be concluded that computational inaccuracies were introduced by not including this surface roughness in the simulation setup. It is also apparent from the two topologies presented, that the painting process increased the layer thickness by 45 microns.

4.5 Pressure Transducer Uncertainty

Finally, the measurements taken with the Ashcroft differential pressure transducer need to be analyzed. For all transducer measurements, a 12-bit NI USB-6008 data acquisition unit was used. Over the 2,488 Pa range of the Ashcroft transducer this data acquisition unit allowed for a 0.6075 Pa resolution for all pressure measurements. For both *in-situ* calibration measurements, 120,000 samples were taken leading to a standard error of 0.0257 Pa for the pressure transducer at $Z/L_{cone} = 0.0625$ and a standard error of 0.0460 Pa for the pressure transducer at $Z/L_{cone} = 0.5625$. For pressure measurements over the entire cyclone system a standard error of 0.0321 Pa was calculated. Combining two standard errors for one or both pressure transducers, when appropriate, along with the device resolution via a root-sum-square gives the total uncertainty for the pressure measurements given in Table 4.1.

Table 4.1: Static pressure measurements taken with differential pressure transducer.

Pressure, Pa ($Z/L_{cone} = 0.0625$)	Pressure, Pa ($Z/L_{cone} = 0.5625$)	Δp (Cone), Pa	Δp (System), Pa
1134 $\pm$0.6097	1027 $\pm$0.6092	86.22 $\pm$0.6114	923.8 $\pm$0.6109

Chapter 5. Results and Discussion

5.1 Numerical Results

The cyclone velocity and pressure fields computed from CFD were inspected for the purposes of guiding the experimental program. Where appropriate, comparisons to experimental data from the literature are made. Two different CFD setups were used; one with the "particle outlet" as a pressure outlet at ambient pressure, the other with the "particle outlet" set to a wall boundary condition. These two setups are referred to as "open" and "closed" configuration, respectively. Due to blower limitations the inlet velocity supplied varied based on the cyclone configuration. For the open configuration cyclone, the experimental setup could support an 18 m/s (Q = 0.09 m^3/s) inlet. When operating in the closed configuration the cyclone was supplied a 12 m/s (Q = 0.06 m^3/s) inlet. The CFD results presented are those with which the inlet velocity was equal to the corresponding experimental conditions. The reasoning for implementing two different cyclone configurations is discussed in Sections 5.1.1 and 5.1.2.

5.1.1 Velocity Field

The time-averaged tangential velocity profile computed in this study was compared to experimental data collected via laser Doppler anemometry by Hoekstra [5] for a qualitative assessment of flow trends. The experimental data collected by Hoekstra is not used to benchmark the computational results in this work since various geometric and dynamic parameters differ between the two studies. The Hoekstra experiment was conducted with a Reynolds number (as defined in Equation 1.18) of 280,000 on a typical Stairmand cyclone geometry [5]. The present CFD results — Re = 358,000 and Re = 239,000 for the open and closed configurations, respectively. The experimental data from Hoekstra, and current computational data, are shown in Figure 5.1. The tangential velocity inside a cyclone should exhibit two distinct behaviors dependent on the radial position in the flow field. The inner forced vortex, which follows Equation 1.3, appears to differ between the three sets of data partially as a result of the outlet boundary condition. While the "dust outlet" for the open study is exposed to ambient

conditions, those in many other experiments are attached to collection bins. Having an open system simply permits the flow to exit the cyclone. This creates a cyclone that is absent of any reversed flow through the vortex finder, and therefore eliminates the double vortex structure typically observed in cyclones. The CFD computations for the open case can be referred to as a "once-through" vortex flow, which exhibits a much larger vortex core. This is represented by the wider area of approximately zero tangential velocity displayed in the center of Figure 5.1. With this difference in the flow structure, the tangential velocity trend in the open cyclone displays a distorted version of those commonly seen in the literature.

After modifying the boundary conditions of the experimental model to the closed configuration, the inlet velocity supplied by the blower unit dropped due to a greater load on the system. Likewise, the Reynolds number for the closed configuration calculated using Equation 1.18 was Re = 239,000 as previously mentioned. The tangential velocity for the closed configuration was plotted along the same radial line in Figure 5.1. The large core of extremely low velocity produced from the open configuration is now absent. The presence of a more typical double-vortex, with the inner and outer vortices moving in the positive and negative axial directions, respectively, creates a core forced-vortex with an average diameter much smaller relative to the once-through vortex.

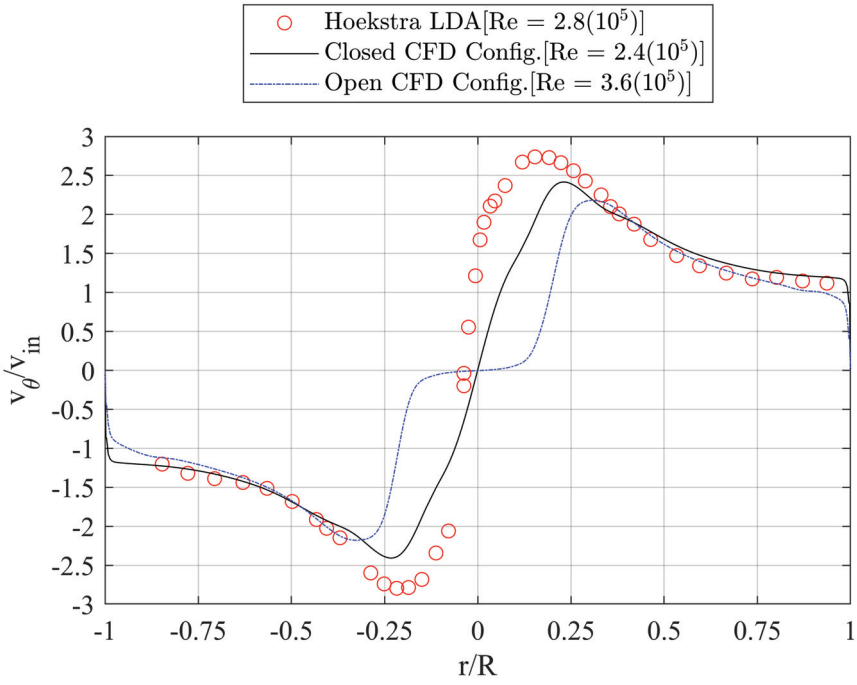

Figure 5.1: Mean tangential velocity profile comparison between literature data [5] and CFD.

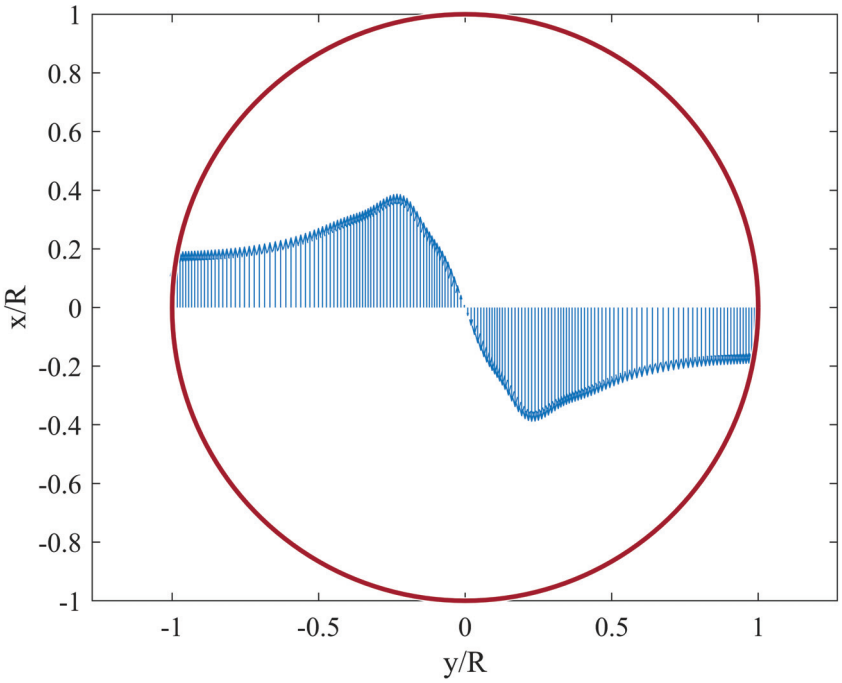

Figure 5.2: Mean X-velocity vectors viewed along Z-axis (closed configuration, Z/R = 0).

Figure 5.1 shows good agreement in flow trends between the experimental and the closed configuration CFD data in regards to the tangential velocity peaks and the free-vortex. The forced-vortex discrepancies between the closed configuration CFD results and the experimental data is most likely explained by the inclusion of a wall-reflection term in pressure strain calculations. A similar phenomenon is reported by Hoekstra [5] in his computational results. He found that the wall-reflection term caused over prediction of the anisotropic stresses near the core, thus creating a noticeable discrepancy between the experimental and computational data. With the open configuration, the maximum tangential velocity was approximately 1.5 times the inlet velocity, while with a closed cyclone the maximum is closer to 2.5 times the inlet velocity. This is closer to expected value, with the tangential velocity generally being at least two times that of the inlet velocity. A plot of the velocity vectors along the same line at $Z/R = 0$ is shown in Figure 5.2. The Rankine character of the flow is clearly displayed again in this representation, with the size of the outer free-vortex accentuated. The velocity profile for the open configuration simulation was modeled with a power fit shown in Figure 5.3, agreeing well with the expected form of Equation 1.2. Although the power power fit for the open configuration follows the form given in Equation 1.2, the closed configuration yields results that are more typical of cyclone separators. Figure 5.4 displays the free-vortex tangential velocity overlaid

with a power fit and the corresponding equation for the closed configuration cyclone. With the closed CFD configuration, the free-vortex follows a power curve with an exponent of 0.58. As mentioned in Section 1.1.2, the exponent defining the shape of the free-vortex curve is typically between 0.5 and 0.8 for cyclone separators [1].

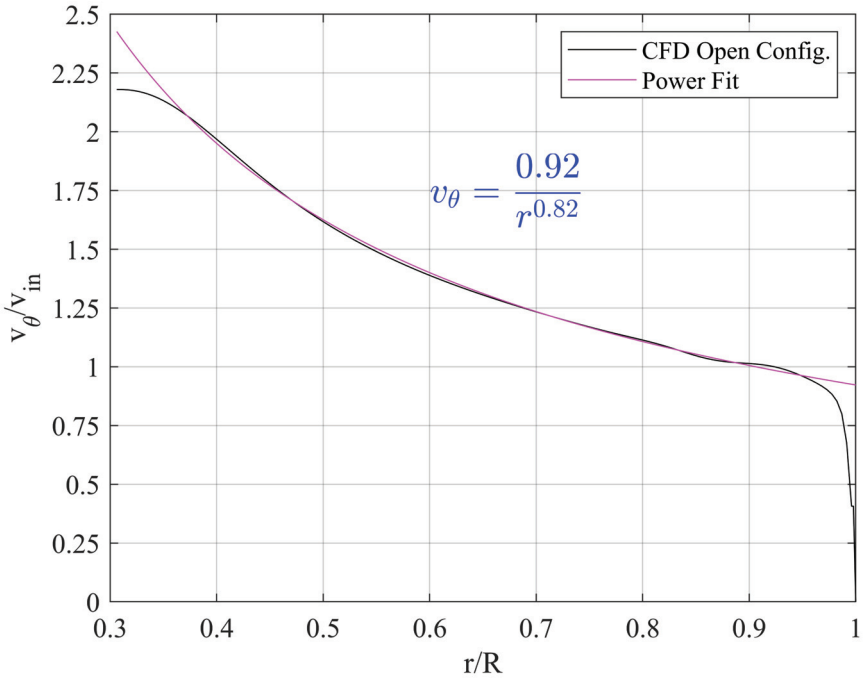

Figure 5.3: Power-curve fitting of free-vortex profile (open configuration, $Z/R = 0$).

Figure 5.5 presents instantaneous tangential velocity contours on the cross-sectional plane of the cyclone. All cross-sectional planes were oriented parallel to the direction of the inlet flow in order to minimize the effects of inlet velocities and accelerations on the contour. The contours clearly depict the expected Rankine vortex structure. The larger vortex core mostly suppresses the vortex core instability and unsteadiness that is typically observed in such contours [14]. The sign of the velocities presented in Figure 5.5 is determined by the angular direction of the flow; conversely, the sign of the velocities presented in Figure 5.1 are determined by a particle's motion relative to the LDA sensor. Consequently, the sign does not change symmetrically about the axis of rotation as it does in Figure 5.1. It is important to take note of the mean direction of the flow field. Based on the geometry, the vortex flow will be in the clockwise direction about the axis or rotation when looking from above the cyclone barrel.

Figure 5.6 illustrates a contour of the instantaneous tangetntial velocity field on the same central plane as Figure 5.5. As with Figure 5.5 the mean rotational direction is in the clockwise direction when looking down the axis of rotation from the top of

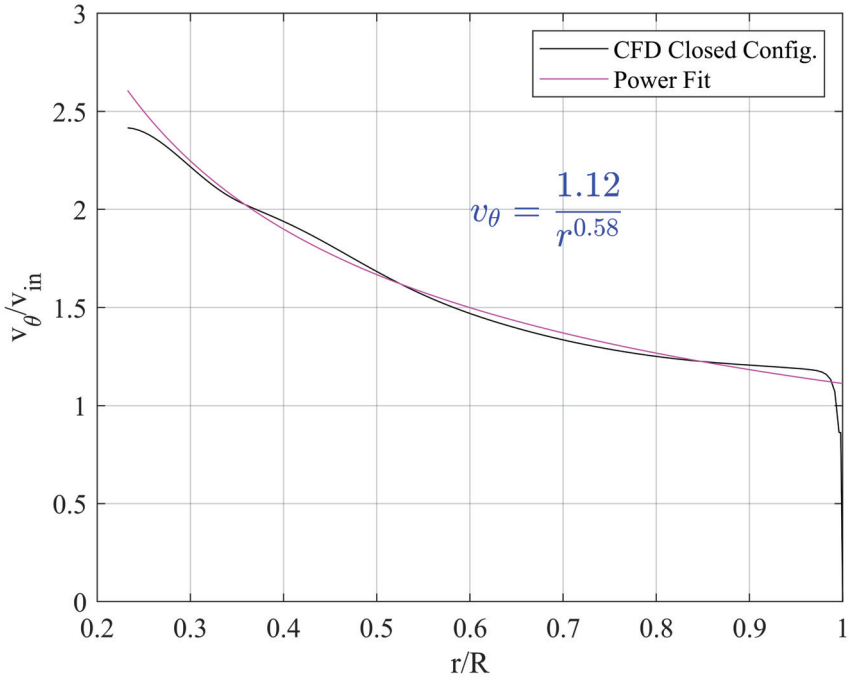

Figure 5.4: Power-curve fitting of free-vortex profile (closed configuration, $Z/R = 0$).

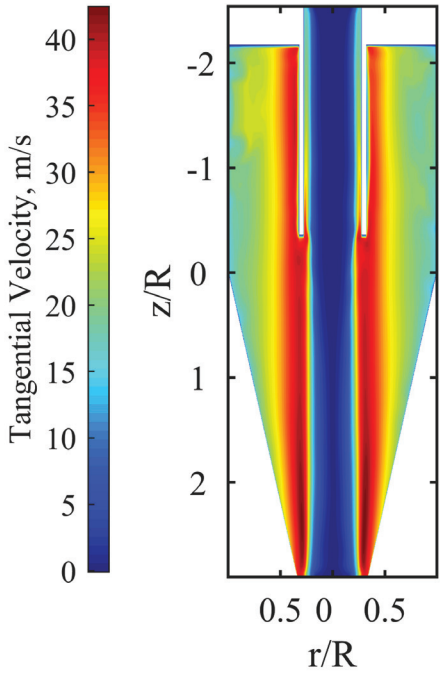

Figure 5.5: Instantaneous tangential velocity contours on central plane (open configuration).

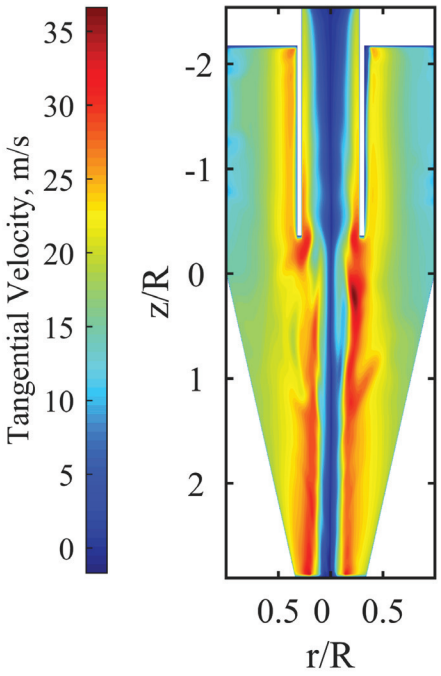

Figure 5.6: Instantaneous tangential velocity contours on central plane (closed configuration).

the cyclone. Figure 5.6 clearly depicts the smaller diameter low velocity core in red. It also displays an unsteady pattern around the edge of the inner forced-vortex. To highlight the unsteady character of the inner forced-vortex, Figure 5.7 presents root-mean-square (RMS) values of the X-component of velocity taken over 3000 time samples. Figure 5.7 shows large spikes in velocity fluctuations at radial locations near the outer edge of the forced-vortex.

Figure 5.8 shows tangential velocity contours on a planes normal to the axis of rotation, while 5.9 displays the Z-vorticity on the same planes. These cut-planes were placed every two inches starting from the particle outlet of the cone. The highest plane in the Z-direction, corresponds to where the cone and barrel meet. These figures highlight two important flow features. First, a periodic pattern in the azimuthal direction is present in the tangential velocity. Figure 5.8 clearly displays the unsteady pattern which appears to be periodic in the azimuthal direction. This unsteadiness at the edge of the inner forced-vortex carries with it the associated vorticity, which will be much higher than that in the outer free-vortex. Thus, a similar pattern appears in Figure 5.9. Artifacts from this phenomenon can be seen in Figure 5.1 and Figure 5.4 by the slight jump in tangential velocity near $y/R = 0.4$. Figures 5.8 and 5.9 help illustrate the three-dimensional flow present in cyclone separators. Other than the unsteady phenomenon occurring at the edge of the forced-vortex,

the tangential velocity and Z-vorticity patterns presented in both contours follow the expected trends. The core-forced-vortex has a high magnitude of vorticity compared to the free-vortex that has a vorticity magnitude near zero.

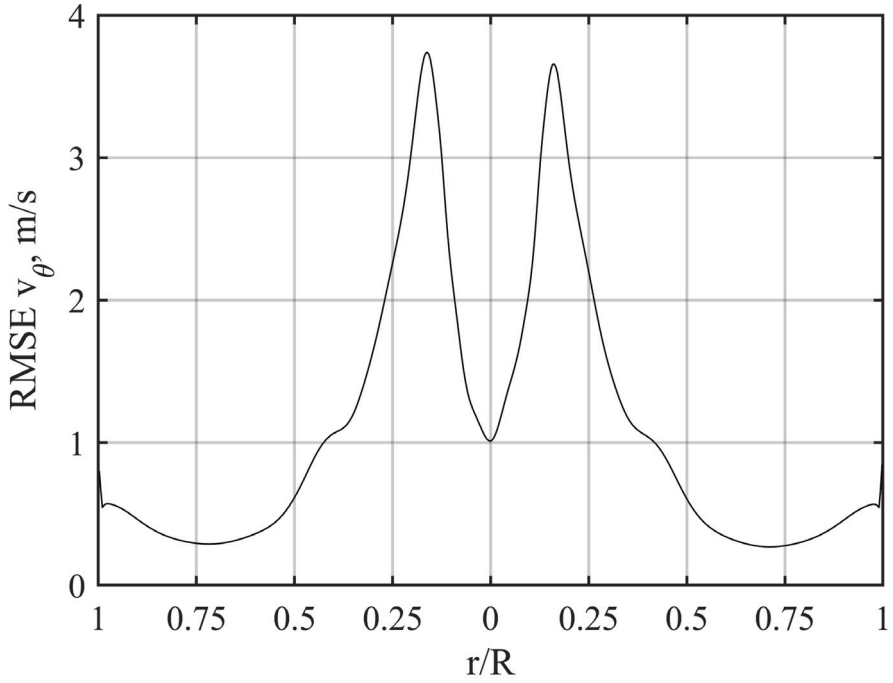

Figure 5.7: RMS X-velocity as function of radial position (closed configuration).

Any unsteady phenomena predicted in RANS simulations should, however, be criticized to a certain extent. As covered in 1.4, the founding principle in any RANS turbulence model is the time-averaging of the Navier-Stokes equations. This inherently dilutes transient flow patterns. Moreover, the helical structure present in Figures 5.8 and 5.9 could be a representation of a truly unsteady pattern rather than the explicit flow solution. To adequately capture this phenomenon, an LES simulation should be considered.

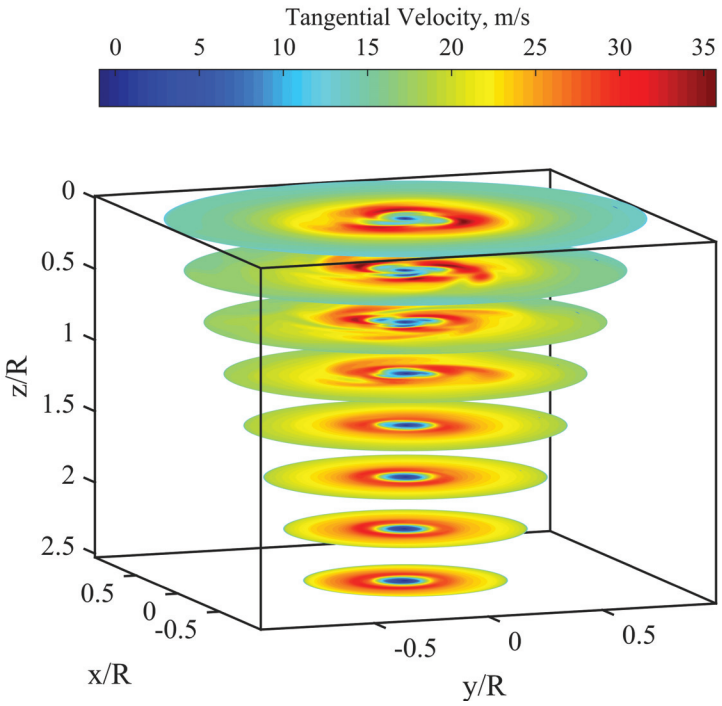

Figure 5.8: Tangential velocity contours on planes normal to axis of rotation (closed configuration).

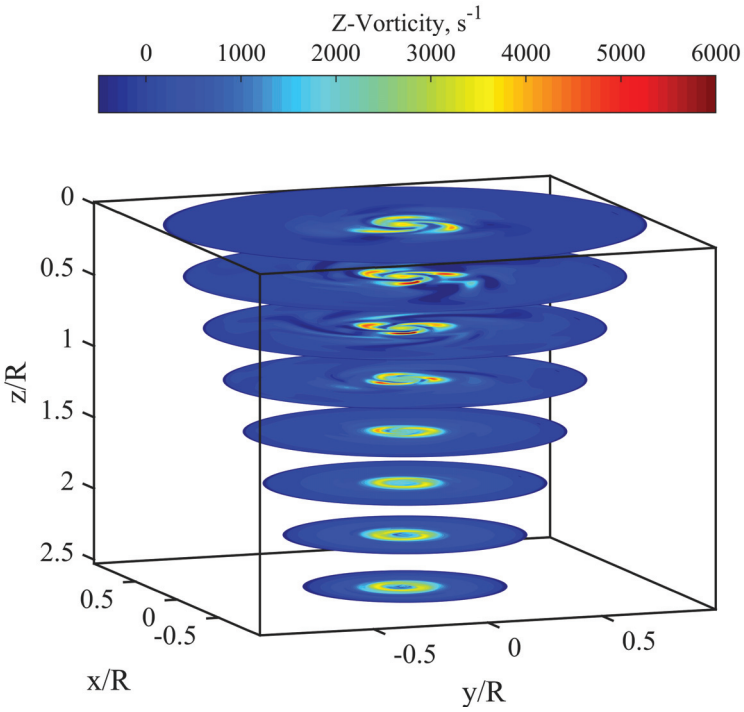

Figure 5.9: Z-vorticity contours on planes normal to axis of rotation (closed configuration).

5.1.2 Pressure Field

While the CFD analysis of the open configuration yielded interesting results in terms of vortex dynamics, an open configuration does not produce an efficient cyclone. As previously mentioned the majority of the flow exits via the "dust exit" along with the dust, and the system as a whole creates vacuum pressures at the end of the vortex finder which pull air into the cyclone rather than exhausting it. To better model the typical industry cyclone separator, additional CFD studies were completed on a cyclone which was closed at the narrow end of the cone. With a wall boundary condition implemented, the vortical flow could no longer exit the apparatus at the end of the cone. Instead the flow reversed axial directions, and, while still maintaining swirl, proceeded up through the vortex finder and exited the cyclone. Many of the same plots and contours were produced to highlight the differences in flow patterns between the opened and closed configurations.

The static pressure should increase in the radial direction as a result of inertial forces. Figure 5.10 presents contours of time-averaged static pressure for the open configuration projected on the same cross-sectional plane as in Figure 5.5. At the cyclone outlets, the vortex core has negative gauge pressure which causes backflow into the cyclone. This is a result of the boundary conditions imposed on the model.

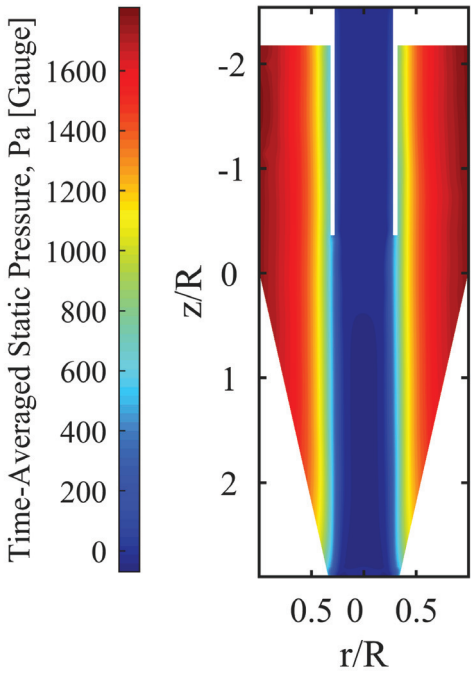

Figure 5.10: Static pressure contours on central plane (open configuration).

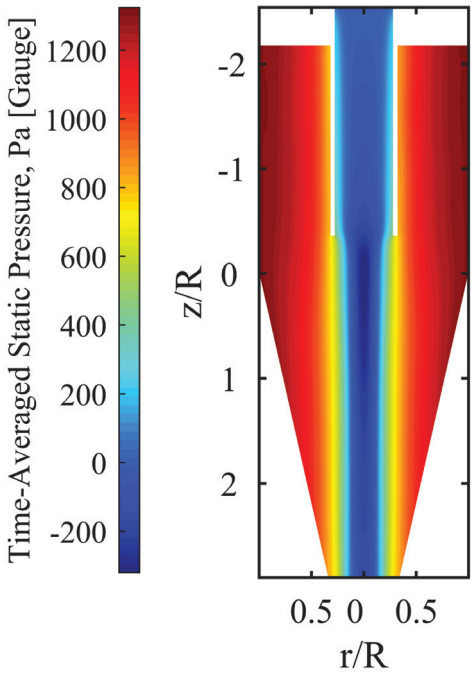

Figure 5.11: Static pressure contours on central plane (closed configuration).

Static pressure values in the closed cyclone yielded results that more closely resemble those found in literature [14]. Figure 5.11 displays time-averaged static pressure on the same central plane as Figure 5.6. As expected the pressure mainly varies with radial distance from the axis of rotation. While the instantaneous pressure field in Figure 5.12 displays unsteadiness near the core, which is coupled to velocity fluctuations, time-averaging of the flow over only a three second period eliminates these fluctuations and presents the axisymmetric pressure field given in Figure 5.11.

To further analyze the pressure distribution in the open configuration cyclone Figure 5.13 displays the static pressure plotted along the radial direction where the cylinder and cone geometries meet (Z/R = 0). The trend displayed corresponds well with trends found in literature [14]. Since the CFD results from the open configuration do not have the inner vortex typically found in most cyclones, static pressure values near zero form a core approximately the diameter of the vortex finder. This is much larger than the low-pressure vortex core found in other work [14].

A similar plot of the radial pressure trend was created for the closed configuration cyclone. The pressure fluctuations present in Figure 5.12 are illustrated in Figure 5.14, which is plotted along the same line as Figure 5.13 at Z/R = 0. The overall trend agrees well with that found the literature [14]. The low pressure core exhibits a much smaller diameter than that found in the open configuration, which is expected due to the coupling between tangential velocity and pressure.

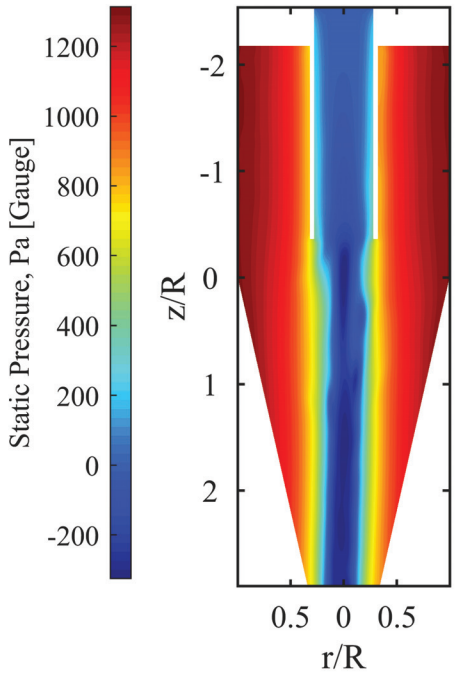

Figure 5.12: Instantaneous static pressure contours on central plane (closed configuration).

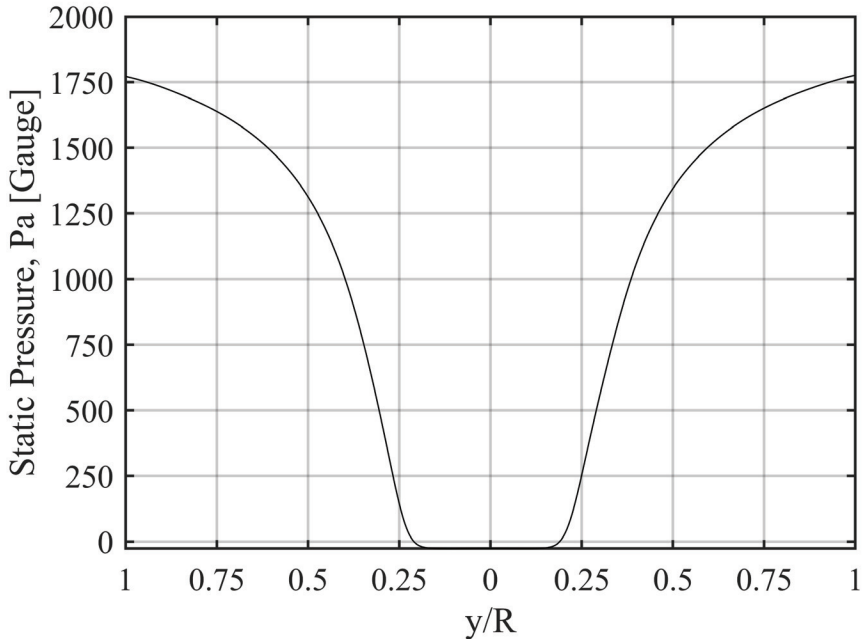

Figure 5.13: Static pressure as function of radial position (open configuration, $Z/R = 0$).

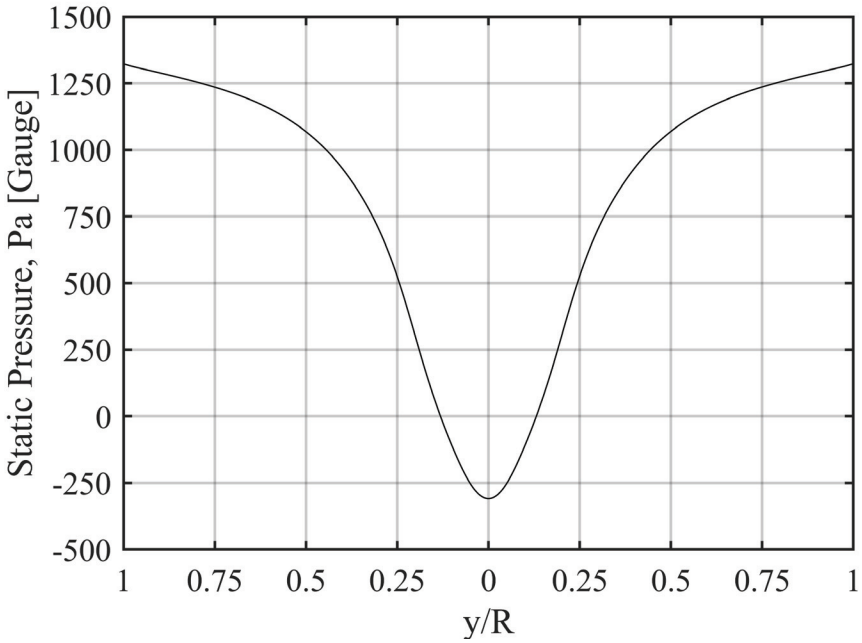

Figure 5.14: Static pressure as function of radial position (closed configuration, $Z/R = 0$).

Using the Shepherd and Lapple model in Equation 1.31 and Equation 1.32 with K = 16, a theoretical pressure drop of 2011 Pa across the open configuration cyclone was calculated. CFD results for the this configuration yielded a pressure drop of 1870 Pa, representing a 7% difference from the conventional model. Along the wall of the cone, a pressure drop of approximately 1200 Pa was calculated for the open model. The pressure drop was calculated across the device again using the Shepherd and Lapple model as before — following Equation 1.31 and Equation 1.32. $K = 16$ was used as recommended yielding a pressure drop of 1964 Pa. The closed configuration CFD model predicted a pressure drop of 1337 Pa across the apparatus resulting in a percent difference of 32%.

While large fluctuations seem to be suppressed by the large vortex core, a degree of unsteadiness was captured in the transient computations. The root-mean-square of the fluctuating static pressure was computed as an indicator of unsteadiness from 2,000 time levels. Figure 5.15 illustrates the fluctuations present near the core of the flow. Most notably, the largest fluctuation levels appear at the radial position corresponding to maximum tangential velocity. When examining instantaneous static pressure in the closed configuration (Figure 5.12), unsteadiness is present near the edge of the core forced-vortex. This unsteadiness corresponding to the velocity fluctuations is present in Figures 5.6, 5.8, and 5.9. These fluctuations are not unexpected as a result of the PVC. Additionally the vortex core is known to support long wave-

length standing waves [32]. To quantify this unsteadiness, RMS values of static pressure were calculated for the closed cyclone simulation. Figure 5.16 displays the RMS values along a radial line at $Z/D = 0$.

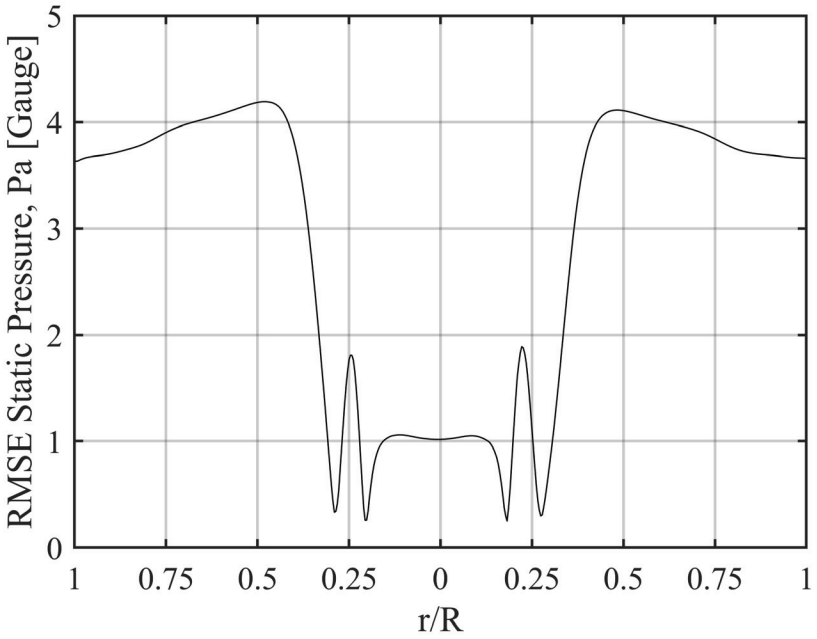

Figure 5.15: RMS of fluctuating pressure as function of radial position (open configuration, $Z/R = 0$).

Figure 5.17 displays the open cyclone time-averaged static pressure contours on the cone wall projected onto a plane in the same manner that PSP images will be recorded (image space vs. object space). As with Figures 5.12 and 5.11 time-averaging the surface pressure map produces axisymmetric results. These data will be valuable for comparison to PSP measurements, which is well-suited for capturing three-dimensional pressure fields.

The pressure distribution along the cone appears to follow a fourth-order polynomial trend. Figure 5.18 displays data sampled along the cone wall with a polynomial fit for the open configuration. The cyclone used for both open and closed configuration studies was designed to induce a large pressure drop over the cone, which is also illustrated in the data. This produces an extremely inefficient cyclone — in the open configuration setup — as the net flow at the clean exit is directed into the cyclone body.

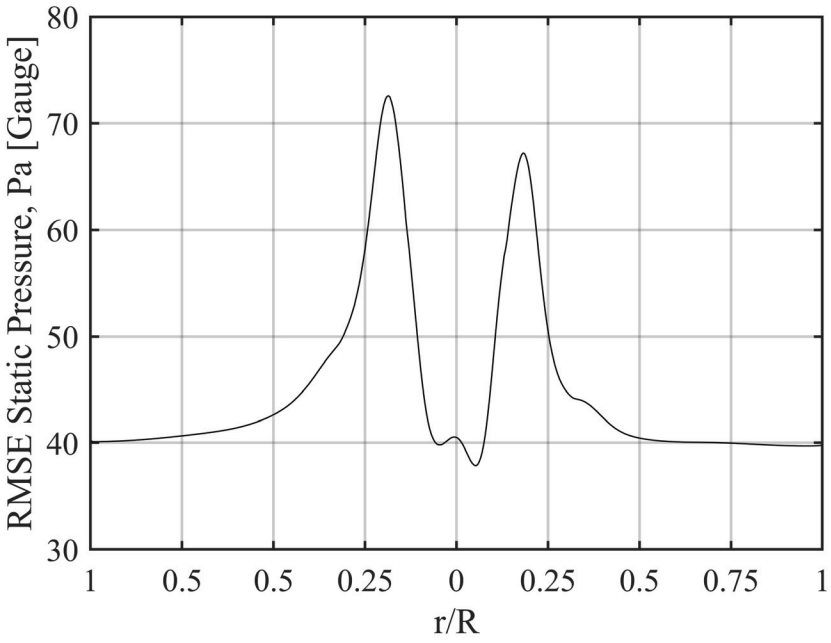

Figure 5.16: RMS static pressure as a function of radial position (closed configuration, $Z/R = 0$).

For comparison to the experimental campaign, static pressure contours were created along the cone wall of the closed cyclone as well. As with Figure 5.17, the static pressure values from the curved cone surface were projected onto a plane. Figure 5.19 depicts these static pressure values. Similarly to the open configuration, the static pressure appears to be axisymmetric since the values have been time-averaged. Relative to the open configuration, the closed cyclone CFD predicts a much smaller pressure drop along the cone surface, which is best illustrated in Figure 5.20.

The difference in pressure drop along the cone between the open and closed configurations is clearly shown in Figures 5.18 and 5.20. A static pressure drop of approximately 1200 Pa was produced in the open cyclone, while the closed cyclone predicted a 440 Pa pressure drop. The pressure drop along the cone wall was best described with a high-order polynomial fit for the open configuration; however, the closed cyclone static pressure trend was characteristic of a power law. The significantly reduced pressure drop along the cone wall was not advantageous for the PSP measurement campaign as it lowered the intensity difference for the camera to capture. Further details are discussed in Section 5.2.

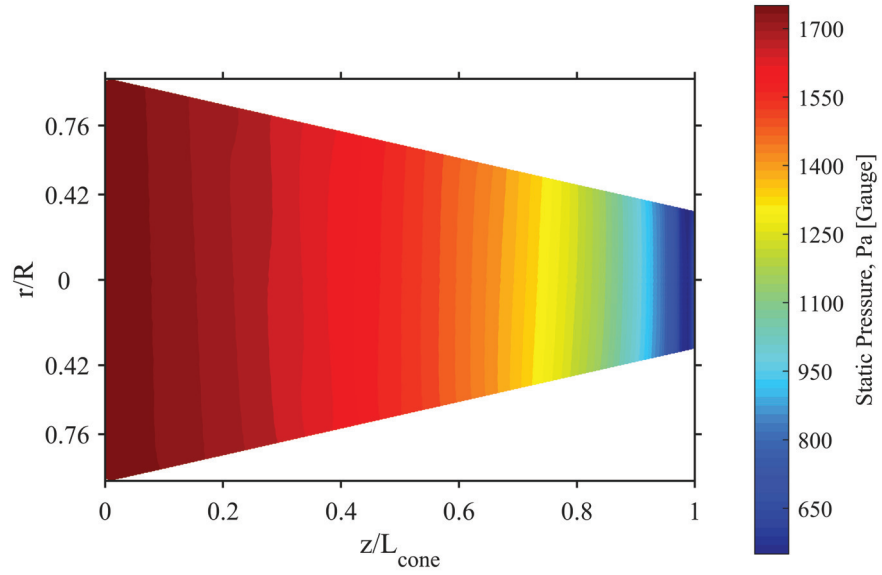

Figure 5.17: Static pressure contours on cone wall from CFD (open configuration).

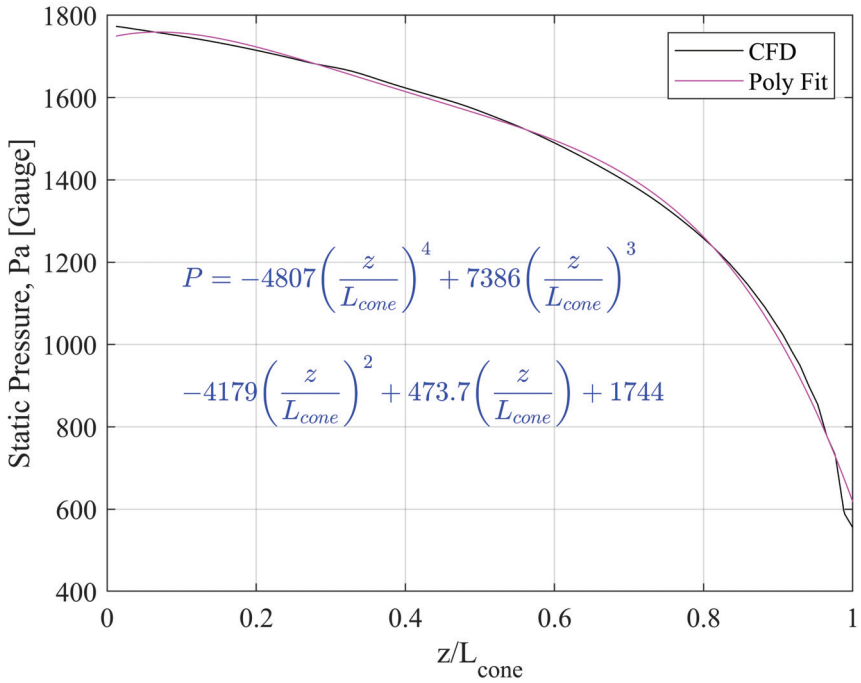

Figure 5.18: Power-curve fitting of static pressure along cone wall (open configuration).

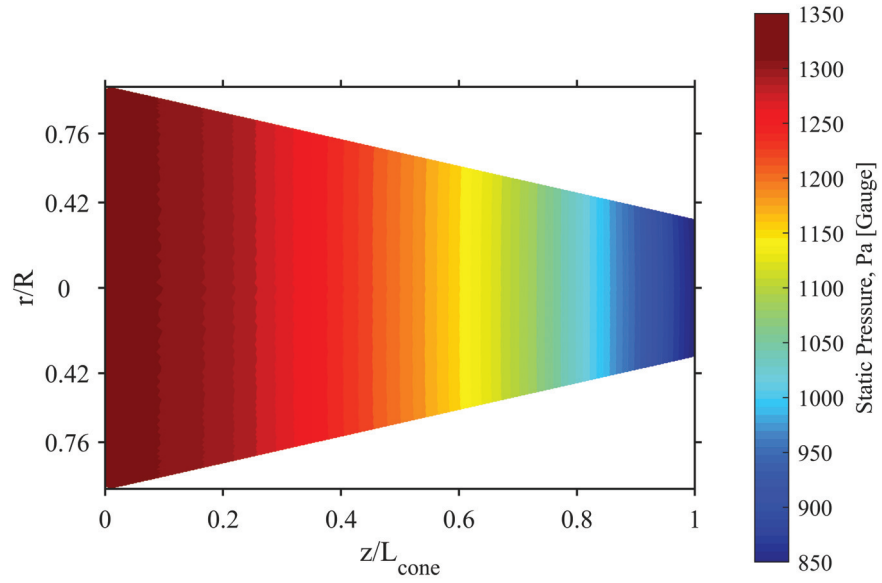

Figure 5.19: Static pressure contours on cone wall from CFD (closed configuration).

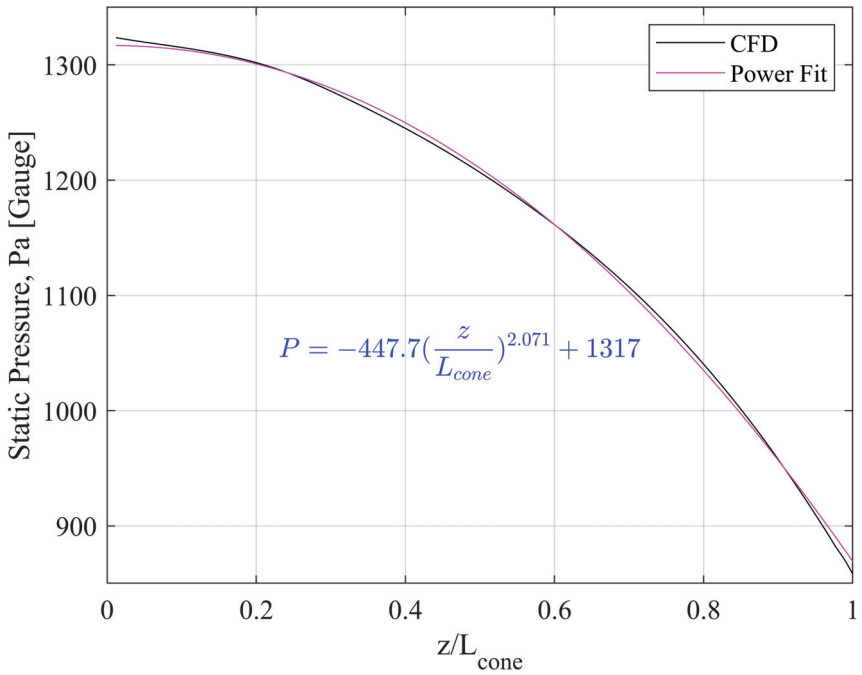

Figure 5.20: Power-curve fitting of static pressure along cone wall (closed configuration).

5.2 Experimental Results

The CFD campaign discussed in Section 5.1 provides valuable assets in characterizing the flow within the cyclone separator; however, the shortcomings accompanying any of the RANS turbulence models cannot be avoided without the added expense of intense computational resources. Details of the assumptions made when implementing RANS turbulence models are outlined in Section 1.4. To mitigate the pitfalls of numerical analysis, experimental analysis was completed on the cyclone separator discussed in this work. While experimental data on cyclone separators is not scarce, the methods by which the data was collected often results in point measurements via techniques that may disrupt the flow. The following experimental measurement campaign was completed using pressure sensitive paint, which, as discussed in Section 1.2, has many advantages. The most prevalent being that the number of virtual pressure taps on the test surface are only limited by pixel density and image resolution.

In this work, images were collected using two-pixel binning resulting in an 800 by 600 pixel image. The binning process allowed a "smoothing" of the intensity images, and provided a higher signal to noise ratio. A total of 256 images were collected for both wind-on and wind-off states as well as for the dark field images (images with the LEDs off to capture ambient background noise). For each state, the images were averaged to create a high signal to noise ratio image for further processing. The accumulation of a large number of images can, however, lend itself to photo-degradation. The effects from photo-degradation were minimized by pulsing the excitation LEDs as discussed in Section 4.1.

To account for image movement and model deflection between the wind-off and wind-on images, image registration was carried out on all wind-on images before processing the data. This was accomplished using four registration points located on the cone surface. Two of the image registration points were created by physical pressure taps and two were marked using a felt-tip marker. The registration marks were kept small in size to reduce the interference with the collected data.

For PSP calibration an *in-situ* calibration was completed for each data set. This was accomplished using two physical pressure taps located along the centerline of the cone. The first pressure tap was located approximately one inch below the start of the cone ($Z/L_{cone} = 0.0625$), and the second was placed eight inches further down the cone towards the narrow end ($Z/L_{cone} = 0.5625$). Using these two pressure taps, time-averaged pressure data was collected over 30 seconds. The two points were then extracted from the intensity ratio matrix and a plot of I_{ref}/I and P/P_{ref} was created. The coefficients determined from the calibration curve were then used as the A and B coefficients required for use in the Stern-Volmer relationship give in Equation 1.46 with $A = 15.03$ and $B = -13.78$. At this point the Stern-Volmer relationship was

solved for P. This new relationship for P was then applied to the intensity ratio matrix to yield the pressure values corresponding to every pixel from the original images. As with all image based measurements, there was an element of noise present in the data. To reduce this noise and produce a more coherent pressure contour, a mean filter with a 10 pixel radius was applied to the intensity ratio matrix before processing.

After processing the filtered intensity ratio matrix, a contour of static pressure was produced which is shown in Figure 5.21. Various areas in Figure 5.21 are shown as "white space" indicating that the region did not produce quality data for processing. The criteria for this masking of the image was set based on intensity values; as such, the registration marks and pressure taps along with the edges of the image, where the curvature of the cone was significant, are masked off. Figure 5.22 is a static pressure contour from the closed configuration CFD cropped to the same size as Figure 5.21. The data collected using the PSP process does not exactly agree with CFD predictions; however, the results are reasonable to compare. The PSP data shows a drop in pressure along the cone wall, as expected, with a slightly different magnitude compared to the CFD results. A slight asymmetry is present in the PSP data that is not shown in the CFD results. From PSP measurements, a pressure drop of approximately 100 Pa is expected along the visible portion of the cone.

To further investigate the asymmetry found in the PSP data, three plots distributed at various "azimuthal" locations are plotted in Figure 5.24. The lines from which the various plot data is extracted are drawn on the PSP image in Figure 5.23. While this investigation shows variance in the azimuthal direction, it should be noted that the proper photogrammetry was not conducted on the PSP image to convert it from image space to object space. Subsequently, the lines of constant "azimuthal" location indicated in Figure 5.23 are approximations based on geometric ratios. Even so, the asymmetry captured with PSP represents the high spatial resolution measurements, which were the main thrust of this work.

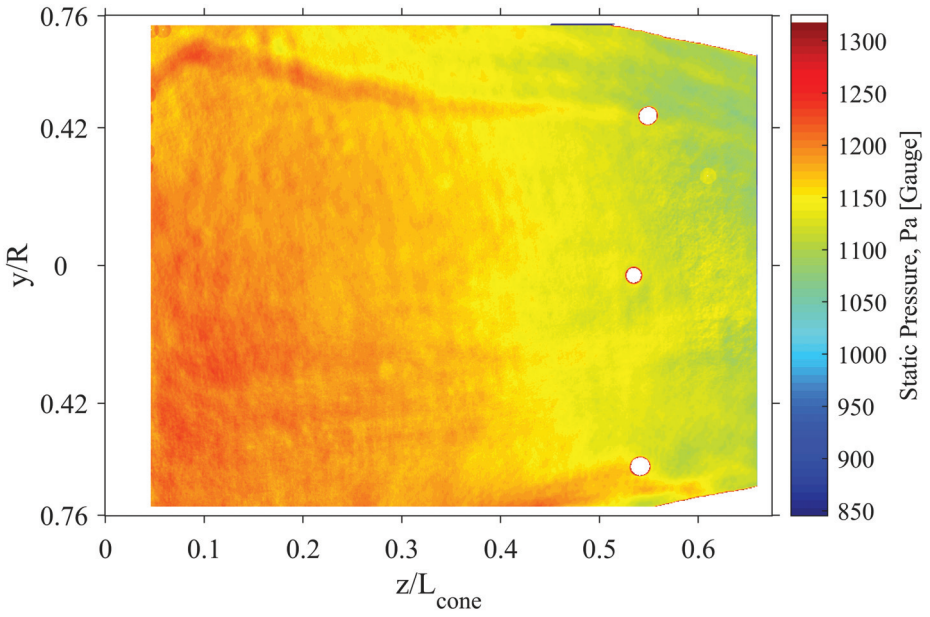

Figure 5.21: Mean static pressure along the cone wall from PSP.

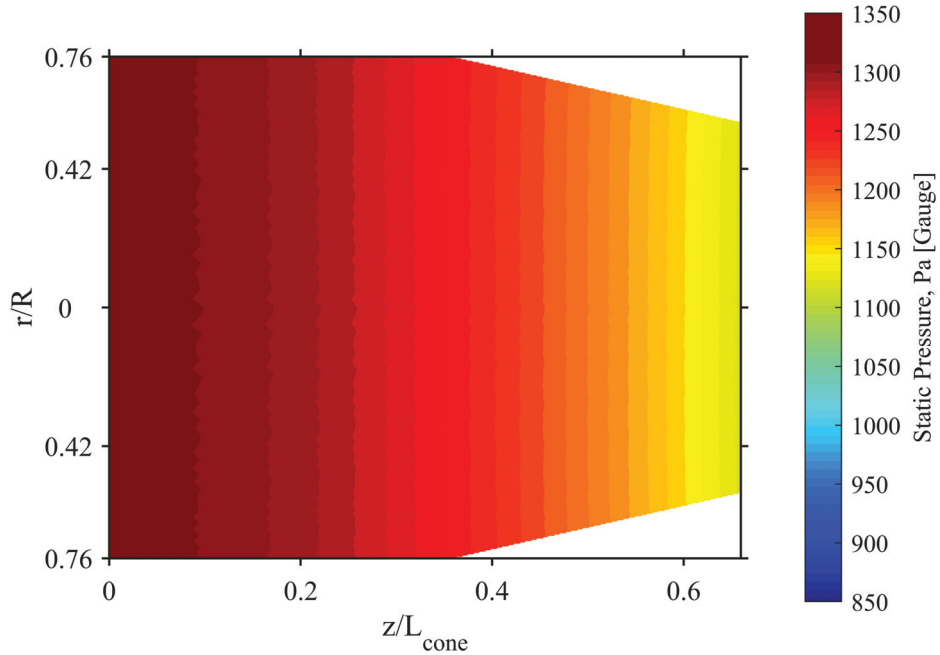

Figure 5.22: Static pressure along the cone wall from close configuration CFD (Cropped to PSP dimensions).

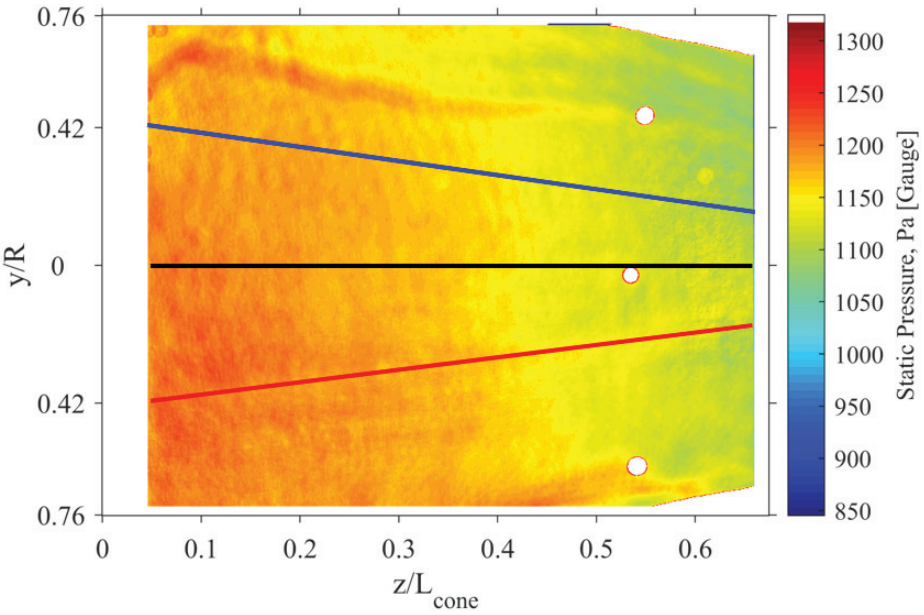

Figure 5.23: PSP static pressure contour indicating plot lines.

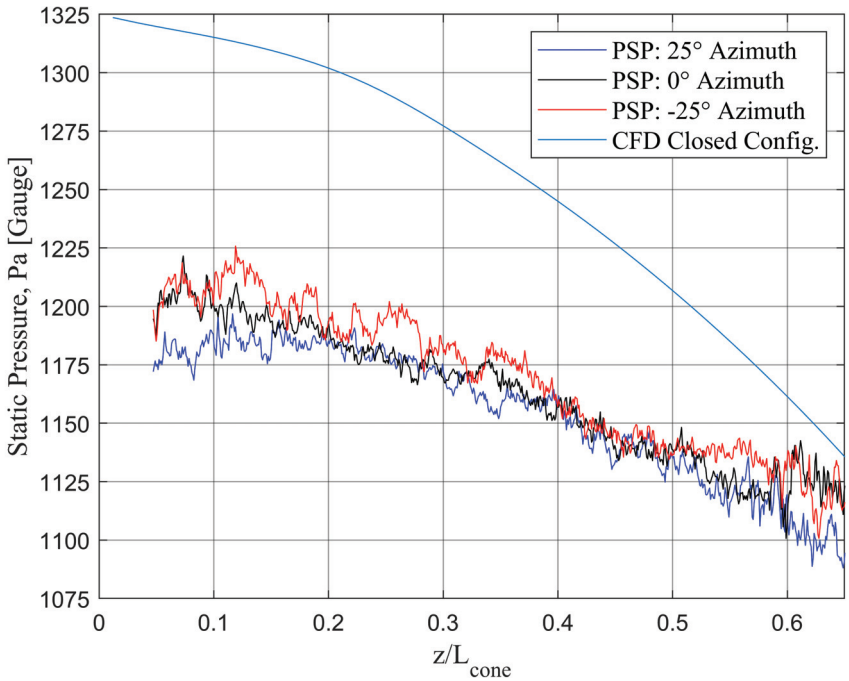

Figure 5.24: Static pressure trend along the cone wall from PSP.

Table 5.1: CFD and experimental pressure measurements and ΔP.

Method	Pressure, Pa ($Z/L_{cone} = 0.0625$)	Pressure, Pa ($Z/L_{cone} = 0.5625$)	Δp (Cone), Pa	Δp (System), Pa
CFD	1317	1173	144	1337
Pressure Taps	1134 $\pm$0.6097	1027 $\pm$0.6092	86.22 $\pm$0.6114	923.8 $\pm$0.6109

In Figures 5.21 and 5.24, the horizontal axis represents the non-dimensional distance in the Z-direction measured relative to where the cone and cylinder sections meet (i.e. $z/L_{cone} = 0$ where the cone and cylinder connect and $z/L_{cone} = 1$ at the particle outlet). Table 5.1 gives pressure data from both CFD and experimental solutions. The data from both methods was acquired at the locations of the physical pressure taps. While a bulk shift in pressure is shown, the magnitude of pressure drop along the cone is comparable for the two techniques. This, however, still produced a 67 % difference between the two techniques. The total pressure drop across the cyclone was measured using pressure taps to be 924 $\pm$0.6109 Pa. This value, compared to the result yielded in CFD of 1337 Pa, produces a percent difference of 45%. In comparison, the pressure drop predicted using the Shepherd and Lapple model (1964 Pa) yielded a percent difference of 113% relative to the experimental measurement. The pressure measured at the vortex finder exit, however, can suffer from inaccuracies due to persistent swirling in the flow, which will give a greater static pressure at the wall and thus a lower total pressure drop across the system. To truly measure the pressure drop across the cyclone separator, a pressure tap would have to be placed far enough downstream of the device such that all swirling motion dissipated before reaching the measurement device.

Clearly shown in Figure 5.24 are discrepancies between the computational and experimental data. A bulk shift in the static pressure expected along the cone wall, as well as a discrepancy in regards to the character of the pressure trend are present. While the CFD follows a power law relation, as shown in Figure 5.20, the pressure drop captured with PSP displays a linear pressure drop along the cone wall. In this representation, the noise captured during the image based measurement is clearly shown in the low amplitude fluctuations. Even so, a general pressure trend along the length of the cone can be established and used for future development.

Chapter 6. Conclusions

6.1 Summary

The data collected for this work came from two different cyclone separator setups, each lending valuable information for future work:

1. The open cyclone design did not produce the desired reverse-flow double vortex typically observed in cyclone separators. This was due to the flow exiting the device at the narrow end of the cone rather than reversing axial directions and exiting via the vortex finder. In this setup, the flow pattern within the cyclone separator developed in such a way as to maximize the volumetric flow rate through the exit. This coincides with the flow expected based on the core pressure drop model [32]. This, produced a Rankine like vortex with a large, low pressure core which, in turn, reduced the maximum tangential velocity of the system. The open configuration CFD predicted a much larger pressure drop along the length of the cone due to modified flow pattern in the system. Compared to the closed configuration CFD, the open configuration produced a pressure drop 273% greater along the cone wall.

2. The closed configuration cyclone separator, with the cone-end blocked, produced the reverse-flow double vortex expected. Furthermore, the flow was forced to exit via the vortex finder thus producing a much smaller diameter vortex core. This flow pattern produced results in CFD that were in good agreement with experimental and CFD data [5, 14]. The flow pattern present in the closed configuration cyclone produced a much lower pressure drop along the length of the cone. This can be partially attributed to the lower inlet velocity of the system. As a result of the higher system load established with the closed cyclone, the experimental apparatus produced and inlet velocity of 12 m/s in the closed cyclone compared to 18 m/s in the open cyclone. The closed configuration (with a lower velocity inlet) caused an unstable forced-vortex core which developed into a helical structure with three-way symmetry about the central axis.

3. Significant photo-degradation was avoided by pulsing the excitation LEDs.

4. The pressure sensitive paint data collected was able to adequately capture the low magnitude pressure drop across the cone wall of the closed configuration separator. By ensemble averaging 256 images to improve signal-to-noise ratio, a static pressure drop trend could be established. While the pressure trend captured does not match that predicted by CFD, the PSP data was able to produce a spatially resolved pressure gradient between the two pressure taps in the device. Discrepancies between the computational and experimental models can be partially accounted for by system leaks in the experimental setup. While the design and intention and the setup was to minimize leaks, some were still present at mating junctions. Additionally, the CFD setup did not take into account boundary layer effects at the inlet. The inlet velocities applied were uniform, which, of course, is not possible in real fluids. The additional vorticity introduced to the system via the boundary layer could have a greater impact on pressure drop than anticipated.

5. The application of pressure-sensitive paint to the interior of the cyclone cone allowed a high spatial resolution pressure map of the cone wall to be created. Capturing the pressure drop along the interior of the cyclone proved the feasibility for further applications of PSP to the complex internal flow in a cyclone separator.

6.2 Future Work and Recommendations

The results from this work can be used as a basis for future investigations into the complex flow in a cyclone separator. The cyclone separator used in this work was fabricated in multiple pieces, which lead to leaks in the system and potential for mating surfaces to be over/under flush. To prevent this, a simpler cyclone made of only two pieces (the barrel and cone) could be produced. To increase the intensity signal from the PSP a cyclone design can be manufactured which allows the current blower system to supply a greater inlet velocity. This will in turn produce a greater pressure drop across the system. To achieve an increased inlet velocity, a new experimental cyclone separator can be made with a smaller internal volume. With sufficient pressure drop and luminescent intensity, the need to average wind-on images could be eliminated, thus allowing for a temporal resolution of the pressure field along the cone wall. A time-resolved pressure field could then lend even greater incite into the understanding of cyclone flow. Along with further PSP measurements, other optical measurement techniques such as Laser-Doppler Velocimetry (LDV) and Particle

Image Velocimetry (PIV) can be conducted utilizing the clear acrylic assembly of the cone. Combining the velocity field data collected with either LDV or PIV along with temporally resolved pressure data at the cone wall could produce detailed data describing any periodic flow structures present in the cyclone separator. Finally, to acquire a more accurate computational solution, the uniform velocity inlet could be replaced by a more realistic velocity profile with boundary layer effects. This would introduce vorticity into the system, which could produce a more accurate flow field and pressure drop solution.

Bibliography

[1] W. Peng, A. Hoffmann, P. Boot, A. Udding, H. Dries, A. Ekker, and J. Kater, "Flow pattern in reverse-flow centrifugal separators," *Powder Technology*, vol. 127, no. 3, pp. 212–222, 2002.

[2] A. C. Hoffmann and L. E. Stein, *Gas cyclones and swirl tubes*, vol. 56. Springer, 2002.

[3] J. H. Bell, E. T. Schairer, L. A. Hand, and R. D. Mehta, "Surface pressure measurements using luminescent coatings," *Annual Review of Fluid Mechanics*, vol. 33, no. 1, pp. 155–206, 2001.

[4] J. Crafton, S. Fonov, L. Goss, E. Jones, and M. Reeder, "Comparison of radiometric and lifetime based pressure-sensitive paints for low speed pressure measurements," in *44th AIAA Aerospace Sciences Meeting and Exhibit*, p. 1041, 2006.

[5] A. Hoekstra, *Gas flow field and collection efficiency of cyclone separators*. PhD thesis, Delft University of Technology, Netherlands, 2000.

[6] T.-C. Hsiao, D.-R. Chen, L. Li, P. Greenberg, and K. W. Street, "Development of a multi-stage axial flow cyclone," *Aerosol Science and Technology*, vol. 44, no. 4, pp. 253–261, 2010.

[7] K. M. Crosby, J. Agui, C. Pennington, E. Sorensen, E. Martin, I. Fritz, and B. Frye, "Measurements of the collection efficiency of an air cyclone in lunar gravity," 2009.

[8] D. Winfield, M. Cross, N. Croft, D. Paddison, and I. Craig, "Performance comparison of a single and triple tangential inlet gas separation cyclone: a cfd study," *Powder Technology*, vol. 235, pp. 520–531, 2013.

[9] W. E. Ranz, "Wall flows in a cyclone separator: A description of internal phenomena," *Aerosol science and technology*, vol. 4, no. 4, pp. 417–432, 1985.

[10] R. McK, "Fundamentals of cyclone design and operation," *Proc. Aust. Inst. Mining Met.*, vol. 152, p. 203, 1949.

[11] W. Barth, "Design and layout of the cyclone separator on the basis of new investigations," *Brenn. Warme Kraft*, vol. 8, no. 1, p. 9, 1956.

[12] E. Muschelknautz, "Die berechnung von zyklonabscheidern für gase," *Chemie Ingenieur Technik*, vol. 44, no. 1-2, pp. 63–71, 1972.

[13] E. Muschelknautz, "Theorie der fliehkraftabscheider mit besonderer berücksichtigung hoher temperaturen und drücke," *VDI-Berichte*, vol. 363, pp. 49–60, 1980.

[14] K. Elsayed and C. Lacor, "The effect of cyclone inlet dimensions on the flow pattern and performance," *Applied mathematical modelling*, vol. 35, no. 4, pp. 1952–1968, 2011.

[15] E. Muschelknautz and M. Trefz, "Druckverlust und abscheidegrad in zyklonen vdi-wärmeatlas 6," *Auflage: Lj1-Lj9*, 1991.

[16] P. Meißner and F. Löffler, "Zur berechnung des strömungsfeldes im zyklonabscheider," *Chemie Ingenieur Technik*, vol. 50, no. 6, pp. 471–471, 1978.

[17] H. Mothes, "Prediction removal in cyclone separators," *Int. Chem. Engng.*, vol. 28, pp. 231–240, 1988.

[18] R. F. Reydon and W. Gauvin, "Theoretical and experimental studies of confined vortex flow," *The Canadian Journal of Chemical Engineering*, vol. 59, no. 1, pp. 14–23, 1981.

[19] A. Ogawa, "Separation of particles from air and gases," 1984.

[20] A. Ogawa, "Mechanical separation process and flow patterns of cyclone dust collectors," *Applied Mechanics Reviews*, vol. 50, no. 3, pp. 97–130, 1997.

[21] M. Bloor and D. Ingham, "Theoretical aspects of hydrocyclone flow," *Progress in Filtration and Separation*, vol. 3, pp. 57–148, 1983.

[22] M. Bloor and D. Ingham, "A theoretical investigations of the fluid mechanics of the cyclone," *Proceedings of the Filtration Society*, vol. 21, pp. 266–269, 1984.

[23] M. Bloor and D. Ingham, "The flow in industrial cyclones," *Journal of Fluid Mechanics*, vol. 178, pp. 507–519, 1987.

[24] D. Kelsall, "A study of the motion of solid particles in a hydraulic cyclone," 4 1952.

[25] L. Svarovsky, *Hydrocyclones*. Technomic Pub Co, 1984.

[26] D. Ingham and L. Ma, "Predicting the performance of air cyclones," *International Journal of Energy Research*, vol. 26, no. 7, pp. 633–652, 2002.

[27] T. J. Overcamp and S. E. Scarlett, "Effect of reynolds number on the stokes number of cyclones," *Aerosol science and technology*, vol. 19, no. 3, pp. 362–370, 1993.

[28] A. K. Gupta, D. G. Lilley, and N. Syred, "Swirl flows," *Tunbridge Wells, Kent, England, Abacus Press, 1984, 488 p.*, 1984.

[29] R. C. Chanaud, "Observations of oscillatory motion in certain swirling flows," *Journal of Fluid Mechanics*, vol. 21, no. 1, pp. 111–127, 1965.

[30] D. G. Sloan, P. J. Smith, and L. D. Smoot, "Modeling of swirl in turbulent flow systems," *Progress in Energy and Combustion Science*, vol. 12, no. 3, pp. 163–250, 1986.

[31] M. Escudier, "Confined vortices in flow machinery," *Annual Review of Fluid Mechanics*, vol. 19, no. 1, pp. 27–52, 1987.

[32] J. L. Smith, *Experimental and analytical study of the vortex in the cyclone separator*. PhD thesis, Massachusetts Institute of Technology, 1959.

[33] T. ITO, Y. SUEMATSU, N. KANDA, and T. HAYASE, "On the oscillatory phenomena in a swirling pipe flow: 1st rep. experiments on the precession of the vortex," *Bulletin of JSME*, vol. 26, no. 218, pp. 1348–1356, 1983.

[34] J. Lopez, "Axisymmetric vortex breakdown part 1. confined swirling flow," *Journal of Fluid Mechanics*, vol. 221, pp. 533–552, 1990.

[35] G. Brown and J. Lopez, "Axisymmetric vortex breakdown part 2. physical mechanisms," *Journal of Fluid Mechanics*, vol. 221, pp. 553–576, 1990.

[36] J. Lopez and A. Perry, "Axisymmetric vortex breakdown. part 3 onset of periodic flow and chaotic advection," *Journal of Fluid Mechanics*, vol. 234, pp. 449–471, 1992.

[37] A. Y. Gelfgat, P. Bar-Yoseph, and A. Solan, "Stability of confined swirling flow with and without vortex breakdown," *Journal of Fluid Mechanics*, vol. 311, pp. 1–36, 1996.

[38] J. Derksen and H. Van den Akker, "Simulation of vortex core precession in a reverse-flow cyclone," *AIChE Journal*, vol. 46, no. 7, pp. 1317–1331, 2000.

[39] P. Jochmann, A. Sinigersky, M. Hehle, O. Schäfer, R. Koch, and H.-J. Bauer, "Numerical simulation of a precessing vortex breakdown," *International Journal of Heat and Fluid Flow*, vol. 27, no. 2, pp. 192–203, 2006.

[40] F. Ficici, V. Ari, and M. Kapsiz, "The effects of vortex finder on the pressure drop in cyclone separators," *International Journal of Physical Sciences*, vol. 5, no. 6, pp. 804–813, 2010.

[41] C. Shepherd and C. Lapple, "Flow pattern and pressure drop in cyclone dust collectors cyclone without intel vane," *Industrial & Engineering Chemistry*, vol. 32, no. 9, pp. 1246–1248, 1940.

[42] K. J. Caplan, "Source control by centrifugal force and gravity," *AC Stern, Academic Press, New York*, vol. 11, p. 247, 1962.

[43] C. Stairmand, "Pressure drop in cyclone separators," *Engineering*, vol. 168, no. 4369, p. 409, 1949.

[44] J. W. Gregory, H. Sakaue, T. Liu, and J. P. Sullivan, "Fast pressure-sensitive paint for flow and acoustic diagnostics," *Annual Review of Fluid Mechanics*, vol. 46, pp. 303–330, 2014.

[45] B. E. Carroll, J. D. Abbitt, E. W. Likas, and M. J. Morris, "Step response of pressure-sensitive paints," *AIAA journal*, vol. 34, no. 3, pp. 521–526, 1996.

[46] V. Mosharov, V. Radchenko, and S. Fonov, "Luminescent pressure sensors in aerodynamic experiment, moscow: Cent," *Aerohydrodynamic Inst.(TsAGI). CWA International Corp*, vol. 151, 1997.

[47] N. A. Winslow, B. F. Carroll, and A. J. Kurdila, "Model development and analysis of the dynamics of pressure-sensitive paints," *AIAA journal*, vol. 39, no. 4, pp. 660–666, 2001.

[48] T. Liu and J. Sullivan, *Pressure and Temperature Sensitive Paints*. Springer, 2005.

[49] J. W. Gregory and J. P. Sullivan, "Effect of quenching kinetics on unsteady response of pressure-sensitive paint," *AIAA journal*, vol. 44, no. 3, pp. 634–645, 2006.

[50] H. Sakaue, "Porous pressure sensitive paints for aerodynamic applications," *MS Thesis, School of Material Science and Engineering, Purdue University*, 1999.

[51] H. Sakaue, T. Tabei, and M. Kameda, "Hydrophobic monolayer coating on anodized aluminum pressure-sensitive paint," *Sensors and Actuators B: Chemical*, vol. 119, no. 2, pp. 504–511, 2006.

[52] J. Gregory, K. Asai, M. Kameda, T. Liu, and J. Sullivan, "A review of pressure-sensitive paint for high-speed and unsteady aerodynamics," *Proceedings of the Institution of Mechanical Engineers, Part G: Journal of Aerospace Engineering*, vol. 222, no. 2, pp. 249–290, 2008.

[53] H. Sakaue, "Luminophore application method of anodized aluminum pressure sensitive paint as a fast responding global pressure sensor," *Review of Scientific Instruments*, vol. 76, no. 8, p. 084101, 2005.

[54] H. Sakaue and K. Ishii, "A dipping duration study for optimization of anodized-aluminum pressure-sensitive paint," *Sensors*, vol. 10, no. 11, pp. 9799–9807, 2010.

[55] H. Sakaue and K. Ishii, "Optimization of anodized-aluminum pressure-sensitive paint by controlling luminophore concentration," *Sensors*, vol. 10, no. 7, pp. 6836–6847, 2010.

[56] H. Zare-Behtash, L. Yang, N. Gongora-Orozco, K. Kontis, and A. Jones, "Anodized aluminium pressure sensitive paint: effect of paint application technique," *Measurement*, vol. 45, no. 7, pp. 1902–1905, 2012.

[57] H. Sakaue, K. Morita, Y. Iijima, and Y. Sakamura, "Response time scales of anodized-aluminum pressure-sensitive paints," *Sensors and Actuators A: Physical*, vol. 199, pp. 74–79, 2013.

[58] A. Scroggin, E. Slamovich, J. Crafton, N. Lachendro, and J. Sullivan, "Porous polymer/ceramic composites for luminescence-based temperature and pressure measurement," *MRS Online Proceedings Library Archive*, vol. 560, 1999.

[59] J. Gregory, H. Sakaue, and J. Sullivan, "Unsteady pressure measurements in turbomachinery using porous pressure sensitive paint," in *40th AIAA Aerospace Sciences Meeting & Exhibit*, p. 84, 2002.

[60] H. Tanji, "Photophysical properties of platinum tetra (pentafluorophenyl)-porphyrin in liquid and fib polymer," *Chemistry*, vol. 499, 1998.

[61] E. Puklin, B. Carlson, S. Gouin, C. Costin, E. Green, S. Ponomarev, H. Tanji, and M. Gouterman, "Ideality of pressure-sensitive paint. i. platinum tetra (pentafluorophenyl) porphine in fluoroacrylic polymer," *Journal of Applied Polymer Science*, vol. 77, no. 13, pp. 2795–2804, 2000.

[62] J. N. Demas, "Photophysical pathways in metal complexes," *Journal of Chemical Education*, vol. 60, no. 10, p. 803, 1983.

[63] R. UIBEL, G. Khalil, M. Gouterman, J. Gallery, and J. CALLIS, "Video luminescent barometry-the induction period," in *31st Aerospace Sciences Meeting*, p. 179, 1993.

[64] M. Gouterman, "Oxygen quenching of luminescence of pressure sensitive paint for wind tunnel research," *Journal of Chemical Education*, vol. 74, no. 6, p. 697, 1997.

[65] J. R. Lakowicz, *Principles of fluorescence spectroscopy*. Springer Science & Business Media, 2013.

[66] ANSYS Fluent, *Fluent Theory Guide 19.1*, 2018.

[67] W. Jones and A. Pascau, "Calculation of confined swirling flows with a second moment closure," *Journal of Fluids Engineering*, vol. 111, no. 3, pp. 248–255, 1989.

[68] J. Houben, C. Weiss, E. Brunnmair, and S. Pirker, "Cfd simulations of pressure drop and velocity field in a cyclone separator with central vortex stabilization rod.," *Journal of Applied Fluid Mechanics*, vol. 9, no. 1, 2016.

[69] D. C. Wilcox *et al.*, *Turbulence modeling for CFD*, vol. 2. DCW industries La Canada, CA, 1998.

[70] G. Gronald and J. Derksen, "Simulating turbulent swirling flow in a gas cyclone: A comparison of various modeling approaches," *Powder technology*, vol. 205, no. 1-3, pp. 160–171, 2011.

[71] H. Safikhani, M. Akhavan-Behabadi, M. Shams, and M. Rahimyan, "Numerical simulation of flow field in three types of standard cyclone separators," *Advanced Powder Technology*, vol. 21, no. 4, pp. 435–442, 2010.

[72] J. Derksen, "Simulations of confined turbulent vortex flow," *Computers & Fluids*, vol. 34, no. 3, pp. 301–318, 2005.

[73] L. Liu, H. Dou, X. Chen, and H. Zhang, "Analysis of vortex flow in a cyclone separators based on the energy gradient theory," in *IOP Conference Series: Materials Science and Engineering*, vol. 72, p. 042037, IOP Publishing, 2015.

[74] S. Rajmistry, S. Ganguli, P. Chandra, P. K. Chatterjee, *et al.*, "Numerical analysis of gas-solid behavior in a cyclone separator for circulating fluidized bed system.," *Journal of Applied Fluid Mechanics*, vol. 10, no. 4, 2017.

[75] T. Chuah, J. Gimbun, and T. S. Choong, "A CFD study of the effect of cone dimensions on sampling aerocyclones performance and hydrodynamics," *Powder technology*, vol. 162, no. 2, pp. 126–132, 2006.

[76] T. Bencic, "Calibration of detection angle for full field pressure-sensitive paints measurements," in *39th Aerospace Sciences Meeting and Exhibit*, p. 307, 2001.